



HAL
open science

Deciphering Fast Ion Transport in Glasses: A Case Study of Sodium and Silver Vitreous Sulfides

Mohammad Kassem, Tinehinane Bounazef, Anton Sokolov, Maria Bokova, Daniele Fontanari, Alex Hannon, Igor Alekseev, Eugene Bychkov

► **To cite this version:**

Mohammad Kassem, Tinehinane Bounazef, Anton Sokolov, Maria Bokova, Daniele Fontanari, et al.. Deciphering Fast Ion Transport in Glasses: A Case Study of Sodium and Silver Vitreous Sulfides. Inorganic Chemistry, 2022, 61 (32), pp.12870-12885. 10.1021/acs.inorgchem.2c02142 . hal-04217125

HAL Id: hal-04217125

<https://ulco.hal.science/hal-04217125>

Submitted on 7 Feb 2024

HAL is a multi-disciplinary open access archive for the deposit and dissemination of scientific research documents, whether they are published or not. The documents may come from teaching and research institutions in France or abroad, or from public or private research centers.

L'archive ouverte pluridisciplinaire **HAL**, est destinée au dépôt et à la diffusion de documents scientifiques de niveau recherche, publiés ou non, émanant des établissements d'enseignement et de recherche français ou étrangers, des laboratoires publics ou privés.

Deciphering Fast Ion Transport in Glasses: a Case Study of Sodium and Silver Vitreous Sulfides

Mohammad Kassem,¹ Tinehinane Bounazef,¹ Anton Sokolov,¹ Maria Bokova,¹ Daniele Fontanari,¹ Alex C. Hannon,² Igor Alekseev,¹ and Eugene Bychkov^{1*}

¹ Laboratoire de Physico-Chimie de l'Atmosphère, Université du Littoral Côte d'Opale, 59140 Dunkerque, France

² ISIS Facility, Rutherford Appleton Laboratory, Didcot OX11 0QX, U.K.

ABSTRACT

High-capacity solid-state batteries are promising future products for large-scale energy storage and conversion. Sodium fast ion conductors including glasses and glass ceramics are unparalleled materials for these applications. Rational design and tuning of advanced sodium sulfide electrolytes needs a deep insight into the atomic structure and dynamics in relation with ion transport properties. Using pulsed neutron diffraction and Raman spectroscopy supported by first principles simulations, we show that preferential diffusion pathways in vitreous sodium and silver sulfides are related to isolated sulfur S_{iso} , that is, the sulfur species surrounded exclusively by mobile cations with a typical stoichiometry of $M/S_{\text{iso}} \approx 2$. The $S_{\text{iso}}/S_{\text{tot}}$ fraction appears to be a reliable descriptor of fast ion transport in glassy sulfide systems over a wide range of ionic conductivities and cation diffusivities. The S_{iso} fraction increases with mobile cation content x , tetrahedral coordination of the network former and, in case of thiogermanate systems, with germanium disulfide metastability and partial disproportionation, $\text{GeS}_2 \rightarrow \text{GeS} + \text{S}$, leading to formation of additional sulfur, transforming into S_{iso} . A research strategy enabling to achieve extended and interconnected pathways based on isolated sulfur would lead to glassy electrolytes with superior ionic diffusion.

1. INTRODUCTION

Carbon-neutral alternative energy production and consumption implies a wide range of large-scale energy storage and conversion including low-cost stationary and mobile sodium devices and installations. Amorphous and crystalline sodium ternary or complex sulfides belong to promising advanced materials for solid-state batteries.¹⁻³ Rational design of these compounds requires a deep insight into the atomic structure and relationships between the origin of fast ion transport and chemical or structural features. A seminal discovery of cubic Na₃PS₄ with room-temperature ionic conductivity $\sigma_i = 0.2 \text{ mS}\cdot\text{cm}^{-1}$, obtained by crystallization from the glassy state,⁴ has triggered an avalanche of research work in this direction, and numerous sodium sulfides and selenides (Na₃PSe₄, Na₁₀SnP₂S₁₂, Na₃SbS₄, Na₁₁Sn₂PnS₁₂, where Pn = Sb, P; etc.) were reported,⁵⁻¹¹ reaching $\sigma_i = 32 \text{ mS}\cdot\text{cm}^{-1}$ at 298 K.¹⁰ A large majority of superionic sodium chalcogenides consist of isolated PnX₄ and/or TX₄ tetrahedra, where X = S, Se; and T = Si, Ge, Sn, connected by sodium.

Fast Li⁺ and Na⁺ ion transport in superionic solid conductors as Li₁₀GeP₂S₁₂ or Na₃SbS₄ is often associated with 3D diffusion pathways representing either a combination of one-dimensional channels crossing diffusion planes¹² or orthogonal channels, parallel to crystallographic axes.¹³ Nevertheless, superior ionic mobility requires both disorder, as tetragonal remnants in a cubic lattice,¹⁴ and defects (vacancies, interstitials) in the cationic sublattice.⁸⁻¹¹ Aliovalent substitution, when Ge replaces phosphorus in Li-bearing argyrodites, Li_{6+x}P_{1-x}Ge_xS₅I, causes both anionic (S/I) and cationic site disorder,¹⁵ leading to a significant increase in ionic conductivity up to 4 orders of magnitude. A paddle-wheel mechanism,¹⁶ representing a coupling of tetrahedral rotation and cation translation, is also considered as a favorable factor and a research strategy,¹⁷ enabling to achieve even higher ionic conductivity, especially in glassy electrolytes with lower atomic number density.¹⁸ Another approach consists in using systems composed of super-tetrahedral clusters, that is, B₁₀S₂₀, revealing a large void space and accommodating highly disordered alkali and sulfide ions, or alkali-halide pairs forming a 'liquid-like' disordered sublattice with enhanced cation mobility.¹⁹

We should however note that the best Na⁺ superionic solids exhibit room-temperature ionic conductivity comparable or lower than the extrapolated conductivity of *hypothetical* high-temperature Na₂S after experiencing a diffuse second-order phase transition from a regular low-conducting fcc structure to a highly disordered isostructural antifluorite polymorph,^{20,21} see also Figure 1 and related references. Similar trend is observed for vitreous silver sulfides suggesting the chemical and topological origin of preferential diffusion pathways is reminiscent of superionic α -Ag₂S, Figure 1. The only difference between the two families resides in a high-temperature character of the type-II superionic transition at T_c in Na₂S ($T_c/T_m \approx 0.7$ and $T_m = 1442 \text{ K}$) and Ag₂S (a type-I transition, $T_c/T_m \approx 0.4$ and $T_m = 1115 \text{ K}$).²¹ Lithium counterparts reveal an intermediate case; fcc Li₂S has high- T melting, $T_m = 1465 \text{ K}$, but $T_c/T_m \approx 0.5$.²⁰ Basically, similar origin of high ionic conductivity was intensively discussed in the past for silver sulfide and silver iodide glasses based essentially on a double extrapolation: (i) from high to ambient temperatures for α -Ag₂S or α -AgI, and (ii) a compositional extrapolation of ambient $\sigma_i(x)$ to $x = 1$ for glasses. Nevertheless, no direct structural evidence was found except for crystallization of α -AgI on splat or roller quenching in glassy (AgI) _{x} (Ag₃BO₃)_{1- x} , where $0.78 \leq x \leq 0.90$.^{31,32}

High-resolution diffraction studies using spallation neutron sources and/or 3G synchrotron facilities supported by first-principles simulations enable a better understanding of disordered systems. The structural motifs in crystalline references can be compared in details with their glassy counterparts and reveal previously unnoticed structural features. In particular, it was found that the equilibrium phase diagrams only partially reflect short and intermediate range order in the glass systems in addition to expected structural disorder. Primarily, a topological disorder should be mentioned when unexpected structural motifs were discovered in glasses.

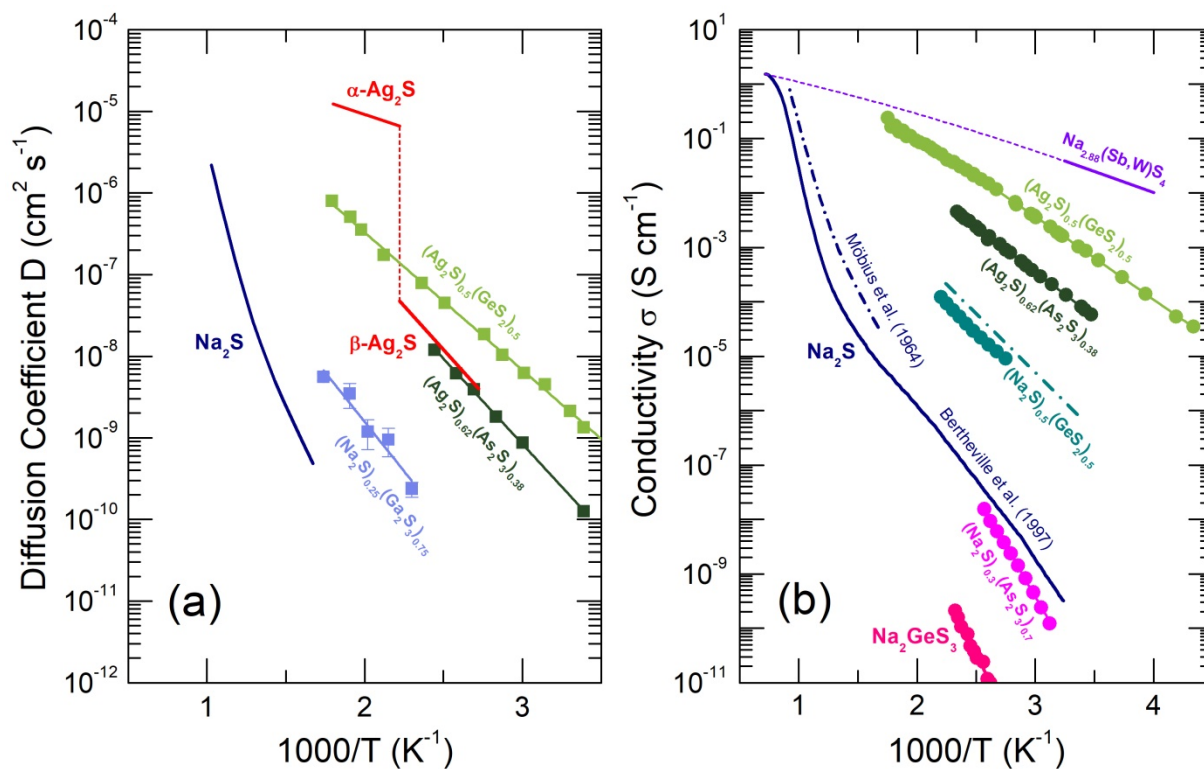


Figure 1. (a) ²²Na and ^{110m}Ag tracer diffusion, and (b) ionic conductivity for benchmark sodium (Na₂S,^{22,23} Na_{2.88}Sb_{0.88}W_{0.12}S₄¹⁰) and silver (Ag₂S²⁴) fast ion conductors and respective sodium and silver thioarsenate, thioarsenate and thiogermanate glasses,²⁵⁻³⁰ as well as monoclinic Na₂GeS₃.²⁸

Sodium and silver, (M₂S)_x(As₂S₃)_{1-x} (M = Na, Ag) and (Ag₂S)_x(GeS₂)_{1-x}, vitreous sulfides, where 0.3 ≤ x ≤ 0.6, exhibit isolated sulfur species S_{iso}, that is, sulfur without direct contacts to arsenic or germanium and only surrounded by silver or sodium with a typical stoichiometry M/S_{iso} ≈ 2.^{29,30} Isolated sulfur is not a unique phenomenon for glassy alloys. In crystalline thioarsenates and thiogermanates, S_{iso} appears above well-defined stoichiometry limits, M₂S/As₂S₃ > 3 ($x > 3/4$) and M₂S/GeS₂ > 2 ($x > 2/3$), when As or Ge concentration is insufficient to ensure connections to all available sulfur. Superionic silver argyrodite Ag₈GeS₆ contains 1/3 of S_{iso} and 2/3 of terminal sulfur S(*t*) species.³³ However, sodium and silver vitreous sulfides violate the stoichiometry rules and equilibrium phase diagrams; the isolated sulfur species appear well below the crystalline limits.

The ionic conductivity and cation diffusion increases as a function of S_{iso}/S_{tot} fraction. Glassy (Ag₂S)_{0.5}(GeS₂)_{0.5} and (Ag₂S)_{0.625}(As₂S₃)_{0.375} have identical silver content, 33.3 at.% Ag, but their ^{110m}Ag tracer diffusion coefficients appear to be different by a factor of 11±2 at room temperature, Figure 1a, coherent with S_{iso}/S_{tot} = 17.6±1.4% (As-glass) and 20.6±1.9% (Ge-glass).²⁹ Vitreous (Na₂S)_{0.3}(As₂S₃)_{0.7} with a modest S_{iso} fraction, 6.2%,³⁰ exhibits a much lower

1
2
3 room-temperature ionic conductivity σ_i compared to more concentrated $g\text{-(Ag}_2\text{S)}_{0.6}\text{(As}_2\text{S}_3)_{0.4}$
4 (the difference in σ_i of 11 orders of magnitude) but also considering sodium thiogallate and
5 thiogermanate glasses with identical Na content (the difference is roughly a factor of 10^4), Figure
6 1b and Figure S1 (Supporting Information). For a detailed analysis, advanced studies of vitreous
7 $(\text{Na}_2\text{S})_x(\text{GeS}_2)_{1-x}$ are required, unraveling the structural and chemical roots of fast ion
8 transport in glasses, in particular, the nature of mobile cations, that of the host glassy matrix, as
9 well as relations with equilibrium phase diagrams and crystalline references. This system was
10 already studied,^{25,34-37} but a combined approach involving pulsed neutron diffraction, Raman
11 spectroscopy, DFT modeling of vibrational properties and first-principles studies of atomic
12 structure and dynamics, related to well-established ion transport properties, is still missing.
13
14
15
16
17

18 2. EXPERIMENTAL AND SIMULATION DETAILS

19
20
21 **2.1. Synthesis.** Glassy sodium thiogermanates, $(\text{Na}_2\text{S})_x(\text{GeS}_2)_{1-x}$ ($0.0 \leq x \leq 0.6$), and crystalline
22 references: $\text{Na}_4\text{Ge}_4\text{S}_{10}$, Na_2GeS_3 , and $\text{Na}_6\text{Ge}_2\text{S}_7$, were obtained by direct synthesis of metallic
23 sodium (Sigma-Aldrich, 99.9%), sulfur pellets (Alfa Aesar, 99.999%), and previously synthesized
24 glassy GeS_2 placed in vitreous carbon crucibles in evacuated silica tubes. The tubes were heated
25 slowly to 1125-1300 K depending on x , maintained at this temperature for 24-72 h with
26 periodic stirring of the melt, and finally quenched in icy salt water. In contrast, the crystalline
27 thiogermanates after high-temperature homogenization were additionally annealed at 950 K for
28 at least two weeks and cooled down slowly to room-temperature. The preparation procedures
29 have been carried out in a glovebox with controlled humidity. Other information related to
30 temperature regimes and synthesis details was reported elsewhere.^{30,38} A Bruker D8 Advance
31 diffractometer was used to verify the crystal structure of the synthesized references, which was
32 found to be coherent with the reported results.³⁹⁻⁴¹
33
34
35

36
37 **2.2. Raman Spectroscopy Measurements.** The vibrational properties of sodium
38 thiogermanate glasses and crystals were studied using a LabRAM HR Evolution micro-Raman
39 spectrometer (Horiba Scientific) in the $70\text{-}850\text{ cm}^{-1}$ spectral range with a 785 nm solid state
40 laser as an excitation source. The samples were held in evacuated silica tubes to avoid
41 interactions and hydrolysis with ambient air humidity. Several spectra at different locations
42 were taken for each sample to ensure homogeneity and reproducibility of the Raman results.
43 The spectral background subtraction and data analysis were described in details previously.^{42,43}
44
45

46
47 **2.3. Neutron Diffraction Measurements.** Pulsed neutron diffraction experiments have been
48 carried out at the ISIS spallation neutron source (Rutherford Appleton Laboratory, UK). The
49 GEM diffractometer⁴⁴ was used for these measurements at room temperature in vacuum-tight
50 vanadium containers to avoid hydrogen contamination from atmospheric moisture. No impurity
51 hydrogen signal was detected. The neutron diffraction data were corrected⁴⁵ for background
52 and container scattering, multiple scattering, self-attenuation, and inelasticity (Placzek) effects
53 using the GUDRUN program.⁴⁶ A vanadium–niobium rod was also measured and used for data
54 normalization.
55

56
57 **2.4. Sodium Tracer Diffusion Measurements.** The ^{22}Na tracer (the life-time $t_{1/2} = 2.6027$
58 years, iThemba LABS, Faure, South Africa, radionuclide purity 99.9%) was used for tracer
59 diffusion experiments in a thin-layer geometry. A drop of radioactive $^{22}\text{NaCl/HCl}$ solution (pH 2)
60

1
2
3 was deposited onto one face of the plane-parallel sample, kept there for 25-30 minutes (a typical
4 time for isotopic sodium exchange and sorption), wiped with a filter paper, washed twice with a
5 distilled water and then ethyl alcohol, and dried. The sample was wrapped in aluminum foil,
6 evacuated and sealed in a Pyrex tube at ≈ 1 Pa. The diffusion anneals in a furnace at 448 ± 2 K
7 were from 20 to 55 days and terminated by quenching the samples in air. The sides of the
8 sample parallel to the diffusion direction were ground to eliminate surface diffusion effects. The
9 sample was then sectioned on a parallel grinder. The thickness of each section was determined
10 either from the density, cross-sectional area, and weight change of the sample or by direct
11 thickness measurements. Further details on tracer diffusion are given in Supporting
12 information, including Figures S2 and S3, and were published elsewhere.^{47,48}
13
14
15

16 **2.5. DFT Modeling of Raman Spectra.** The DFT simulations of Raman spectra were carried out
17 using Gaussian 16 software.⁴⁹ The structural optimization and harmonic vibrational frequency
18 calculations were realized for size-limited Ge-S, Na-S and Na-Ge-S clusters: Ge_4S_4 , S_2Na_2 , S_2Na_3 ,
19 GeS_4Na_4 , $\text{Ge}_2\text{S}_6\text{Na}_2\text{H}_3$, $\text{Ge}_2\text{S}_6\text{Na}_4$, $\text{Ge}_2\text{S}_7\text{Na}_6$, $\text{Ge}_3\text{S}_9\text{Na}_6$, $\text{Ge}_3\text{S}_{10}\text{Na}_6\text{H}_2$, and $\text{Ge}_4\text{S}_{10}\text{Na}_4$. The Becke
20 three-parameter hybrid exchange functional⁵⁰ and the Lee–Yang–Parr correlation functional
21 (B3LYP)⁵¹ were used for DFT simulations. The small-core relativistic pseudopotential basis set
22 (cc-pVTZ-PP)⁵² and the effective core potentials⁵³ were applied for cluster geometry
23 optimization and calculations of harmonic vibrations. Most of the structures were optimized
24 using the tight convergence option, ensuring adequate convergence and reliability of computed
25 wavenumbers. An extra quadratically convergent self-consistent field procedure⁵⁴ was used for
26 difficult convergence cases. Further details of the DFT simulations are published elsewhere.^{55,56}
27
28
29

30 **2.6. First-Principles Molecular Dynamics (FPMD) Simulations.** The Born–Oppenheimer
31 molecular dynamics implemented within the CP2K package⁵⁷ was used for structural modeling
32 of glassy $(\text{Na}_2\text{S})_{0.5}(\text{GeS}_2)_{0.5}$. The generalized gradient approximation (GGA) and the PBE0 hybrid
33 exchange–correlation functional^{58,59} combining the exact Hartree–Fock and DFT approaches
34 were used. The van der Waals dispersion corrections D3BJ⁶⁰ were also applied, reported to have
35 a positive effect for sodium-containing materials and chalcogenide systems.^{61,62} Basically, the
36 FPMD technique was similar to that reported previously.^{63,64} The initial atomic configurations
37 were created and optimized using the RMC_POT++ code⁶⁵ in comparison with the experimental
38 neutron structure factor $S_N(Q)$ to reach a good agreement. The size of the cubic simulation box,
39 containing 450 atoms (150 Na, 75 Ge and 225 S), was chosen to match the experimental number
40 density. Further optimization was carried out using DFT, applying the molecularly optimized
41 correlation consistent polarized triple-zeta valence basis set TZVP along with the norm-
42 conserving relativistic Goedecker–Teter–Hutter-type pseudopotentials.⁶⁶ FPMD simulations
43 were performed using a canonical *NVT* ensemble with a Nosé–Hoover chain of length 3 as a
44 thermostat. The simulation boxes were heated from 300 K to 600 K (a supercooled liquid state)
45 using 100 K steps for 8-10 ps each. At 600 K, the systems were equilibrated for 13 ps and cooled
46 down to 300 K using the same temperature steps but with a longer simulation time (15-20 ps).
47 Final equilibration and data collection at 300 K were performed for 20 ps. The connectivity and
48 ring statistics were analyzed using the R. I. N. G. S. package⁶⁷ and a modified connectivity
49 program.⁶⁸ The pyMolDyn code⁶⁹ applying the Dirichlet–Voronoi tessellation was used for the
50 calculation of microscopic voids and cavities.
51
52
53
54
55
56
57
58
59
60

3. RESULTS AND DISCUSSION

3.1. Raman Spectroscopy. Typical Raman spectra of the $(\text{Na}_2\text{S})_x(\text{GeS}_2)_{1-x}$ glasses, $0 \leq x \leq 0.6$, are shown in Figure 2. Their comparison with the spectra of crystalline sodium thiogermanates of similar or identical chemical composition is given in Figure 3, together with characteristic crystalline motifs in the $\text{Na}_2\text{S-GeS}_2$ system.^{39-41,70,71} Increasing the sodium sulfide content x , one observes characteristic changes in vibrational properties of both glasses and crystals. The A_1 symmetric in-phase Ge-S breathing in corner-sharing CS-GeS_4 tetrahedra^{55,72-74} remains the most intense vibrational component over the composition range $x \leq 0.5$ but monotonically shifts to lower frequencies from 343 cm^{-1} ($x = 0$) to 328 cm^{-1} ($x = 0.6$), Figure 2b, suggesting an increase in Ge-S interatomic distances. In contrast, the A_1^c companion in-phase Ge-S breathing mode in edge-sharing ES-GeS_4 tetrahedra at 373 cm^{-1} disappears progressively with increasing x , indicating a significant reduction in population of the ES-units, consistent with exclusively corner-sharing connectivity in crystalline sodium thiogermanates, Figure 3b.

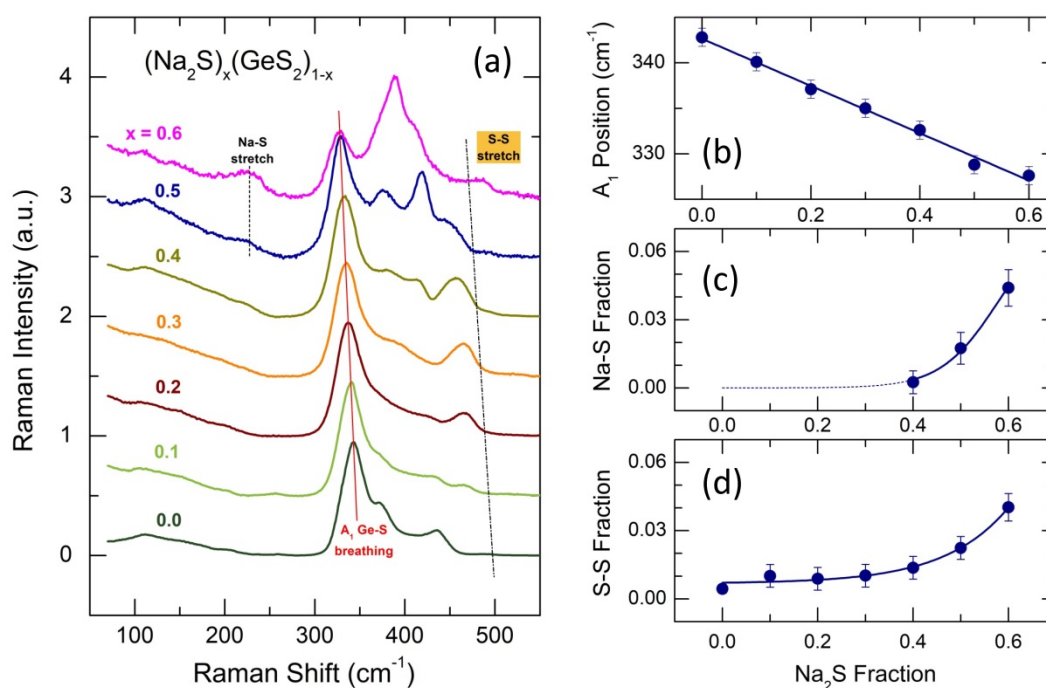


Figure 2. (a) Raman spectra of $(\text{Na}_2\text{S})_x(\text{GeS}_2)_{1-x}$ glasses; the A_1 symmetric in-phase Ge-S breathing mode is emphasized by the red solid line, the emerging Na-S stretching at $\approx 220 \text{ cm}^{-1}$ is indicated by the black dashed line, multiple S-S stretching vibrations are located above 460 - 490 cm^{-1} (the dashed-dotted line); composition dependences of (b) the A_1 symmetric Ge-S breathing frequency, and fractional areas of (c) the Na-S and (d) the S-S stretching modes. See text for further details.

Figure 3a reveals the main spectroscopic features are similar in the glasses and crystals, consistent with previous reports,²⁵ although remarkable differences still exist. Sodium-poor glasses, $x \leq 0.3$, seem to contain adamantane units, $\text{Ge}_4\text{S}(b)_6\text{S}(t)_4$, where $\text{S}(t)$ and $\text{S}(b)$ are terminal and bridging sulfur, respectively, reflected by emerging and growing high-frequency unresolved symmetric and asymmetric Ge-S(t) stretching modes centered at $\approx 465 \text{ cm}^{-1}$, also confirmed by DFT modeling, Figure 4e and Table S1 (Supporting information). The adamantane cages, that is, super-tetrahedra consisting of four CS-GeS_4 entities and held together by sodium cations, Figure 3b, represent an essential motif in orthorhombic $\text{Na}_4\text{Ge}_4\text{S}_{10}$.³⁹ The shorter Ge-S(t) distances, $2.139 \pm 0.004 \text{ \AA}$ vs. $2.225 \pm 0.021 \text{ \AA}$ for Ge-S(b), explain a high-frequency shift of the Ge-

$S(t)$ modes. The most intense A_1 in-phase Ge-S breathing of adamantane cages cannot be distinguished from the A_1 counterpart of glassy GeS_2 , as well as the respective Ge-S breathing vibrations of higher sodium thiogermanates, Na_2GeS_3 and $\text{Na}_6\text{Ge}_2\text{S}_7$.^{40,41}

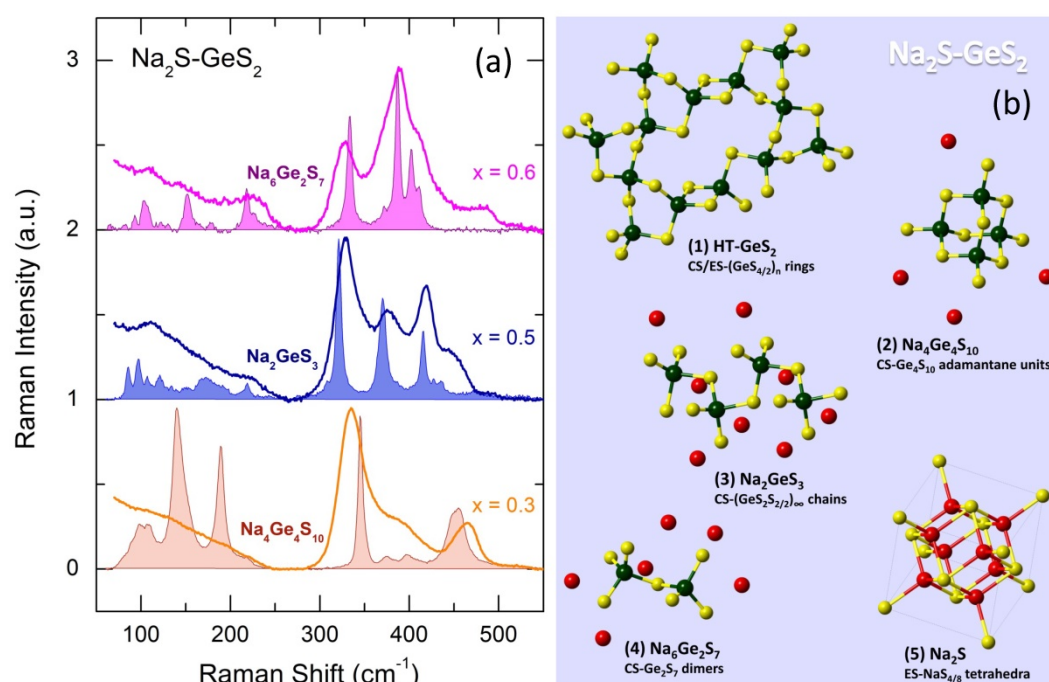


Figure 3. (a) Raman spectra of $(\text{Na}_2\text{S})_x(\text{GeS}_2)_{1-x}$ glasses and crystals with similar or identical chemical composition: $x = 0.3$ and $\text{Na}_4\text{Ge}_4\text{S}_{10}$ ($x = 1/3$), $x = 0.5$ and Na_2GeS_3 ($x = 1/2$), $x = 0.6$ and $\text{Na}_6\text{Ge}_2\text{S}_7$ ($x = 3/5$); (b) crystalline motifs in the $\text{Na}_2\text{S}-\text{GeS}_2$ system: (1) high-temperature monoclinic HT- GeS_2 polymorph consisting of edge- and corner-sharing ES-/CS- $\text{GeS}_{4/2}$ tetrahedra,⁷⁰ (2) orthorhombic tetrasodium closodecathiotetragermanate $\text{Na}_4\text{Ge}_4\text{S}_{10}$, formed by adamantane Ge_4S_{10} units connected by sodium,³⁹ (3) sodium catena-trithiogermanate Na_2GeS_3 , consisting of infinite CS- $(\text{GeS}_2\text{S}_{2/2})_\infty$ chains, where sodium resides in the interchain spaces,⁴⁰ (4) sodium heptathiodigermanate $\text{Na}_6\text{Ge}_2\text{S}_7$, formed by CS- Ge_2S_7 dimers and connected by Na species,⁴¹ and finally (5) face centered cubic fcc- Na_2S , built-up by ES- $\text{Na}_{4/8}$ tetrahedra.⁷¹

As expected, the dominant separated adamantane units are gradually replaced by CS- $[\text{GeS}(t)_2\text{S}(b)_{2/2}]_\infty$ chains at $0.3 \leq x \leq 0.5$, evidenced by two arising mid-frequency vibration features at ≈ 378 and ≈ 416 cm^{-1} , corresponding to poorly resolved symmetric and asymmetric Ge-S stretching involving bridging and terminal sulfur, respectively. The DFT Raman spectrum of the optimized CS- $\text{Ge}_3\text{S}_{10}\text{Na}_6\text{H}_2$ cluster reproduces well the main experimental features of the equimolar $x = 0.5$ glass, Figure 4c. The high-frequency Ge-S(t) stretching exhibits a step-like red shift above $x = 0.3$ from 465 to 438 cm^{-1} , Figure S4 (Supporting information), presumably related to increasing Ge-S(t) interatomic distances, as in orthorhombic $\text{Na}_4\text{Ge}_4\text{S}_{10}$, 2.139 Å, monoclinic Na_2GeS_3 , 2.16 ± 0.02 Å,⁴⁰ and monoclinic $\text{Na}_6\text{Ge}_2\text{S}_7$, 2.192 ± 0.010 Å.⁴¹ Finally, vitreous $(\text{Na}_2\text{S})_{0.6}(\text{GeS}_2)_{0.4}$ at the limit of the glass-forming range reveals the most intense poorly resolved Ge-S stretching modes at ≈ 389 cm^{-1} , similar to pyrothiogermanate $\text{Na}_6\text{Ge}_2\text{S}_7$,⁴¹ consisting of CS- $\text{Ge}_2\text{S}(b)\text{S}(t)_6$ dimers, Figure 3b. Our DFT modeling using CS- $\text{Ge}_2\text{S}_7\text{Na}_6$ clusters shows several symmetric and asymmetric stretching features within this frequency range, involving terminal sulfur species $S(t)$, Figure 4a, Tables S1 and S2.

The crystalline structural motifs alone cannot explain the Raman spectra of glasses entirely. In particular, we note multiple S-S stretching above 460-490 cm^{-1} , whose integrated fractional area $f_{\text{SS}}(\omega)$ increases systematically at $x \geq 0.3$, Figure 2c,

$$f_{\text{SS}}(\omega) = \frac{\int_{\omega_{\text{SS}}}^{\omega_{\text{max}}} I_x(\omega) d\omega}{\int_{\omega_{\text{min}}}^{\omega_{\text{max}}} I_x(\omega) d\omega}, \quad (1)$$

where $I_x(\omega)$ represents the normalized Raman spectrum of a $\text{Na}_2\text{S-GeS}_2$ glass, $460 \text{ cm}^{-1} \leq \omega_{\text{SS}} \leq 490 \text{ cm}^{-1}$ depending on x , $\omega_{\text{min}} = 260 \text{ cm}^{-1}$ and $\omega_{\text{max}} = 600 \text{ cm}^{-1}$. A typical integration procedure is given in Figure S5 (Supporting information) with additional comments.

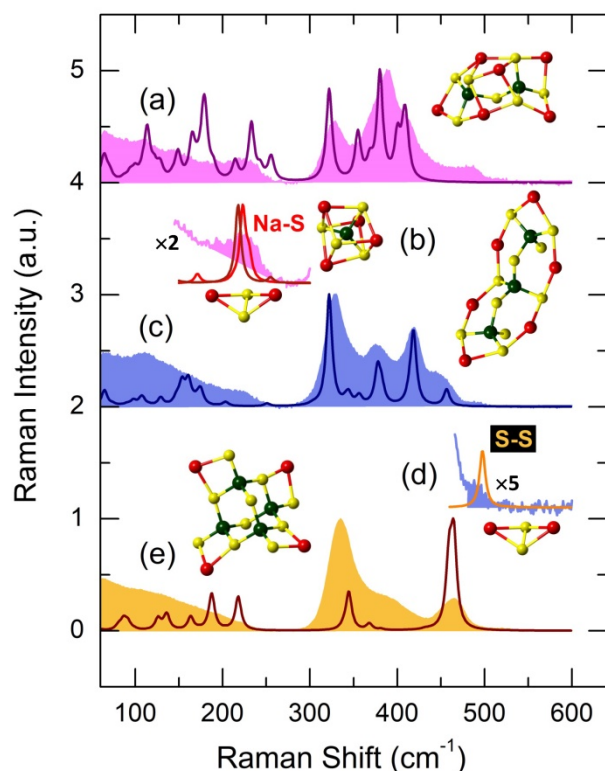


Figure 4. Experimental Raman spectra of $(\text{Na}_2\text{S})_x(\text{GeS}_2)_{1-x}$ glasses and DFT replicas of characteristic vibration features: (a) $x = 0.6$ (highlighted in magenta) and $\text{CS-Ge}_2\text{S}_7\text{Na}_6$ (the purple line), (b) Na-S stretching mode in the $x = 0.6$ glass, and S_2Na_2 (the brown line) and GeS_4Na_4 (the red line) clusters, (c) $x = 0.5$ (highlighted in light blue) and $\text{CS-Ge}_3\text{S}_{10}\text{Na}_6\text{H}_2$ (the dark blue line), (d) S-S stretching mode in the $x = 0.5$ alloy and S_2Na_2 cluster (the orange line), (e) $x = 0.3$ (yellow) and $\text{Ge}_4\text{S}_{10}\text{Na}_4$ cluster (the dark brown line). DFT-optimized Na-Ge-S and Na-S clusters are also shown (the insets). The terminal hydrogen species for $\text{CS-Ge}_3\text{S}_{10}\text{Na}_6\text{H}_2$ are omitted, and the H-related vibrations are removed from the DFT spectrum. See text for further details.

The origins of the S-S stretching are multiple. Stoichiometric glassy matrix GeS_2 shows a small chemical disorder, $2\text{Ge-S} \rightarrow \text{Ge-Ge} + \text{S-S}$. As a result, ethane-like $\text{ETH-Ge}_2\text{S}_6$ units and S-S dimers appear in the glass network detected by Raman spectroscopy⁷⁴⁻⁷⁶ and reproduced by first-principles simulations,^{55,73-74} see also Figure S6 and corresponding text. On the other hand, Raman studies of fcc Na_2S have shown the presence of two S-S stretching modes at 461 and 479 cm^{-1} attributed to polysulfide bridges.⁷⁷ Basically, the S-S stretching modes in crystalline and glassy sodium polysulfides (Na_2S_2 , Na_2S_3 , etc.) are located between 410 and 490 cm^{-1} ,^{78,79} in excellent agreement with our experimental results and DFT simulations. Two types of size-

limited polysulfide clusters were used for DFT modeling: S_2Na_2 , Figure 4d, and S_2Na_3 , Figure S7, representing elements of the structural motifs in α - and β -polymorphs of Na_2S_2 , Figure S7.^{78,79} The S-S stretching frequencies in polysulfide units depend on S-S interatomic distances and vary between 468 cm^{-1} ($r_{SS} = 2.16\text{ \AA}$) and 528 cm^{-1} ($r_{SS} = 2.10\text{ \AA}$).

Sodium-rich glasses, $x > 0.4$, reveal also a rising spectroscopic feature at $\approx 220\text{ cm}^{-1}$ (Figure 2a,c), presumably related to Na-S stretching. Face centered cubic Na_2S shows Raman and IR-active vibrational features between 190 and 220 cm^{-1} ,^{77,80} confirmed by inelastic neutron scattering.⁸¹ In addition, our DFT modeling of Na-S and Na-Ge-S clusters is consistent with this assumption, Figures 4b, S7 and S8, Tables S1 and S2.

3.2. Pulsed Neutron Diffraction. Two Na_2S - GeS_2 glass compositions have been studied using pulsed neutron diffraction: $(Na_2S)_{0.3}(GeS_2)_{0.7}$ and $(Na_2S)_{0.5}(GeS_2)_{0.5}$. The Faber-Ziman neutron structure factors $S_N(Q)$ of the studied sodium thiogermanate glasses are shown in Figure 5 together with that for glassy GeS_2

$$S_N(Q) = \sum_{\alpha,\beta} w_{\alpha\beta}^N S_{\alpha\beta}(Q), \quad (2)$$

and the neutron weighting factors are defined as

$$w_{\alpha\beta}^N = (2 - \delta_{\alpha\beta}) \frac{c_\alpha \bar{b}_\alpha c_\beta \bar{b}_\beta}{|\sum_\alpha c_\alpha \bar{b}_\alpha|^2}, \quad (3)$$

where c_α and \bar{b}_α are, respectively, the atomic concentration and the average of the neutron-nucleus scattering length of element α , $\delta_{\alpha\beta}$ is the Kronecker delta function. The derived structure factors are similar to previously reported results, obtained for glasses, prepared by mechanical milling.³⁷

We note a usual decrease of the first sharp diffraction peak (FSDP) at $Q_0 \approx 1\text{ \AA}^{-1}$ with increasing sodium sulfide content x and an increase of the principal peak PP at $Q_1 \approx 2.2\text{ \AA}^{-1}$. The isolated FSDPs obtained using the subtraction procedure^{82,83} are shown in Figure 5a. We note that the FSDP amplitude A_0 has decreased by a factor of ≈ 2 between g- GeS_2 and $(Na_2S)_{0.3}(GeS_2)_{0.7}$ glass but further FSDP reduction is less significant. The FSDP position Q_0 remains nearly invariant, however, the FSDP shape becomes increasingly asymmetric.

Similar trend was observed for the PP amplitude and position. The biggest change in the PP amplitude appears to be between $x = 0$ and $x = 0.3$, while the difference between the two sodium thiogermanate glasses is negligible. The PP position Q_1 is shifted from 2.33 ($x = 0$) to 2.09 \AA^{-1} ($x = 0.3$) while the equimolar glass shows $Q_1 = 2.08\text{ \AA}^{-1}$.

The neutron total correlation functions $T_N(r)$, obtained using the Fourier transform with $Q_{\max} = 30\text{ \AA}^{-1}$, are shown in Figure 6,

$$T_N(r) = 4\pi\rho_0 r + \frac{2}{\pi} \int_0^{Q_{\max}} Q [S_N(Q) - 1] \sin Qr M(Q) dQ, \quad (4)$$

where $M(Q)$ is the Lorch modification function and ρ_0 the experimental number density.

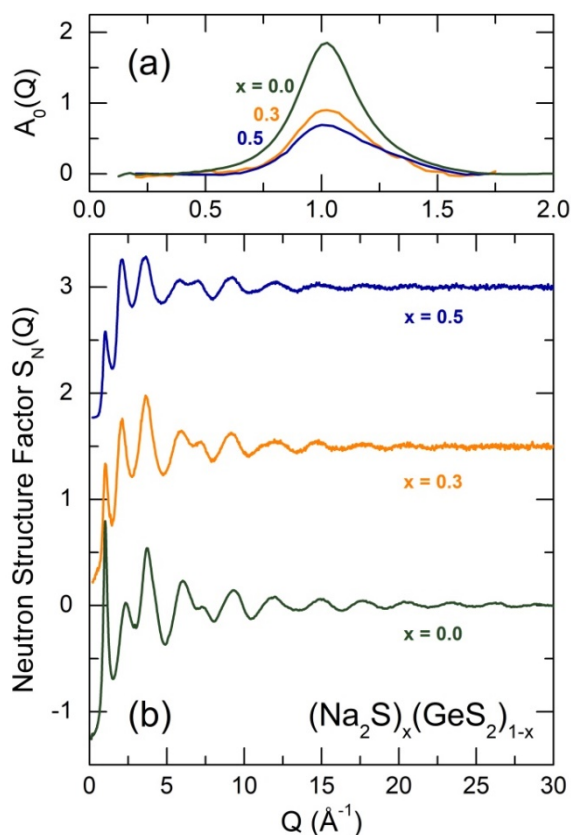


Figure 5. Q -space neutron diffraction data for $(\text{Na}_2\text{S})_x(\text{GeS}_2)_{1-x}$ glasses: $x = 0, 0.3$ and 0.5 ; (a) isolated first sharp diffraction peaks $A_0(Q)$, (b) neutron structure factors $S_N(Q)$. Data for glassy GeS_2 were taken from our previous work.⁸²

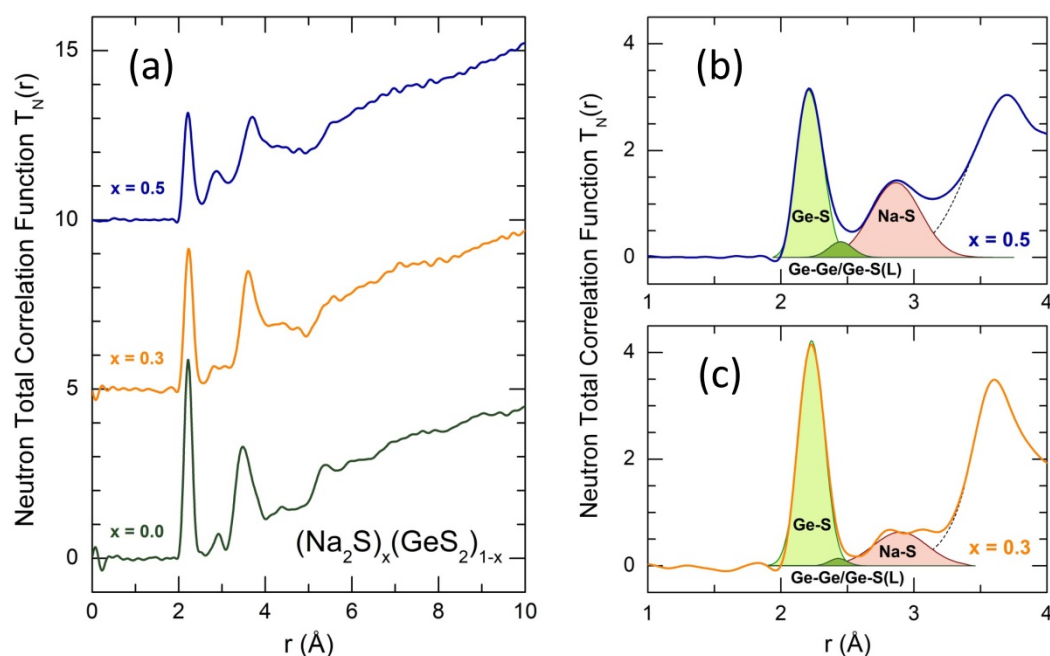


Figure 6. Real-space neutron diffraction data for $(\text{Na}_2\text{S})_x(\text{GeS}_2)_{1-x}$ glasses: $x = 0, 0.3$ and 0.5 ; (a) neutron total correlation functions $T_N(r)$; fitting results for (b) $x = 0.5$ and (c) $x = 0.3$; the nearest neighbor correlations are highlighted: Ge-S (light green), Ge-Ge/Ge-S(L) (green) and Na-S (light red). See text for further details.

The first peak at ≈ 2.2 Å corresponds to Ge-S nearest neighbors.^{37,76,82,84} This peak decreases with x in accordance with stoichiometric relations in $(\text{Na}_2\text{S})_x(\text{GeS}_2)_{1-x}$ glasses, and its position shifts to larger distances (Table 1) indicating a certain expansion of the GeS_2 glass matrix with increasing x . The last trend is also confirmed by a monotonic red shift of the A_1 in-phase Ge-S breathing mode, Figure 2b.

Table 1. Interatomic distances r_{ij} and coordination numbers N_{ij} in $(\text{Na}_2\text{S})_x(\text{GeS}_2)_{1-x}$ glasses derived from the least-square fitting of the experimental data sets and FPMD modeling ($x = 0.5$).

x	S-S		Ge-S		Ge-Ge(1) Ge-S(L)*		Ge-Ge(ES)		Na-S	
	r_{ij} (Å)	N_{ij}	r_{ij} (Å)	N_{ij}	r_{ij} (Å)	N_{ij}	r_{ij} (Å)	N_{ij}	r_{ij} (Å)	N_{ij}
Neutron diffraction										
0	–	–	2.218(5)	3.93(5)	2.43(2)	0.03(2)	2.90(2)	0.49(5)	–	–
0.3	–	–	2.231(5)	3.65(5)	2.43(2)	0.07(4) 0.09(5)*	–	–	2.90(5)	4.1(3)
0.5	–	–	2.250(5)	3.46(5)	2.45(2)	0.23(8) 0.33(11)*	–	–	2.86(3)	4.4(2)
FPMD modeling										
0.5	2.10	0.27	2.22**	3.58	2.45**	0.09	3.19	0.27	2.79**	4.5(5)

The 2.44(1) Å peak corresponds either to Ge-Ge(1) first nearest neighbors/Ge-Ge homopolar bonds and/or to long Ge-S(L) distances; Ge-Ge(ES) corresponds to short Ge-Ge second neighbors in edge-sharing ES- GeS_4 tetrahedra; * Ge-S(L) partial coordination number; ** strongly asymmetric peaks.

The second peak in g- GeS_2 at 2.9 Å corresponds to short Ge-Ge second neighbor distances related to edge-sharing ES- GeS_4 tetrahedra. The monoclinic lattice of high-temperature HT- GeS_2 polymorph⁷⁰ is built-up by corner-sharing CS- GeS_4 and edge-sharing ES- GeS_4 units, Figure 3b. Similar situation exists in glassy GeS_2 .^{76,82,84} In sodium thiogermanate glasses, the presence of short Ge-Ge distances is questionable since an emerging new feature appears at ≈ 2.9 Å, related to Na-S nearest neighbors and similar to that in $\text{Na}_2\text{S-As}_2\text{S}_3$ glasses.³⁰ Consequently, this peak may have two contributions: short Ge-Ge second neighbors and Na-S nearest contacts. We note however a decrease of the A_1^c companion mode at 373 cm^{-1} in Raman spectra of thiogermanate glasses, Figure 2a, suggesting less populated edge-sharing units.

The second neighbor peak at 3.5 Å in g- GeS_2 also shifts to higher r with increasing x and appears at 3.7 Å for sodium thiogermanate glasses, confirming the network expansion. More distant features above 5 Å are becoming flat indicating disappearance of the intermediate range order, characteristic of the GeS_2 glassy host, also confirmed by decreasing FSDP.

A close inspection of the asymmetric first neighbor peak shows the presence of an additional feature at ≈ 2.44 Å. This feature in Ge-rich binary sulfide glasses has a dual nature: (a) Ge-Ge first neighbors indicating the presence of a small fraction of homopolar Ge-Ge bonds, or (b) Ge-S(L) long distances with three-fold coordinated sulfur $\text{S}_{3\text{F}}$ and germanium $\text{Ge}_{3\text{F}}$.⁸²

Typical fitting procedure of $T_N(r)$ using Gaussian functions is shown in Figure 6b,c. The fitting results are summarized in Table 1. Two limiting values are given for the 2.44 Å peak, $N_{\text{Ge-Ge}(1)}$ and $N_{\text{Ge-S}(L)}^*$, calculated assuming the absence of long Ge-S(L) or Ge-Ge(1) first neighbors, respectively. The tetrahedral local coordination of germanium, $\text{Ge}_{4\text{F}}$, remains mostly intact, $N_{\text{Ge-X}} \geq 3.7$ or $\text{Ge}_{4\text{F}}$ fraction $\geq 70\%$, where $N_{\text{Ge-X}} = N_{\text{Ge-S}} + N_{\text{Ge-Ge}}$. Nevertheless, the exact

values may change from $N_{\text{Ge-S}} = 3.8$ ($x = 0.5$, $N_{\text{Ge-Ge}(1)} = 0$) to $N_{\text{Ge-X}} = 3.7$ ($x = 0.5$, $N_{\text{Ge-S(L)}} = 0$). The sodium local coordination appears to be $4.1 \leq N_{\text{Na-S}} \leq 4.4$, assuming the absence of ES-tetrahedra with short Ge-Ge second neighbors. We should however note that this value was obtained by direct fitting with symmetric functions. The sodium local environment in crystalline thiogermanates is characterized by a distribution of Na-S distances, and the above approach could lead to underestimated $N_{\text{Na-S}}$. Similar situation was already observed in $\text{Na}_2\text{S-As}_2\text{S}_3$ glasses, requesting an advanced modeling using the first-principles molecular dynamics.³⁰

3.3. FPMD Modeling of $(\text{Na}_2\text{S})_{0.5}(\text{GeS}_2)_{0.5}$. The simulated neutron interference function $Q[S_{\text{N}}(Q) - 1]$ is shown in Figure 7a together with experimental data. The FPMD modeling using hybrid GGA/PBE0 functional describes the obtained neutron diffraction results reasonably well. The oscillation amplitudes and periodicity are in good agreement with the experiment. A typical problem of the small FPMD simulation boxes, related to heavy computational costs, is a lower amplitude of the FSDP and PP at 1.0 and 2.1 \AA^{-1} , respectively. In case of $(\text{Na}_2\text{S})_{0.5}(\text{GeS}_2)_{0.5}$, we also observed a small shift of the PP to higher Q . The experimental and simulated neutron pair-distribution functions $g_{\text{N}}(r)$ are shown in Figure 7d. We also note a good agreement for the nearest neighbors ($r \lesssim 3 \text{ \AA}$) and a slight shift to lower r for more distant correlations.

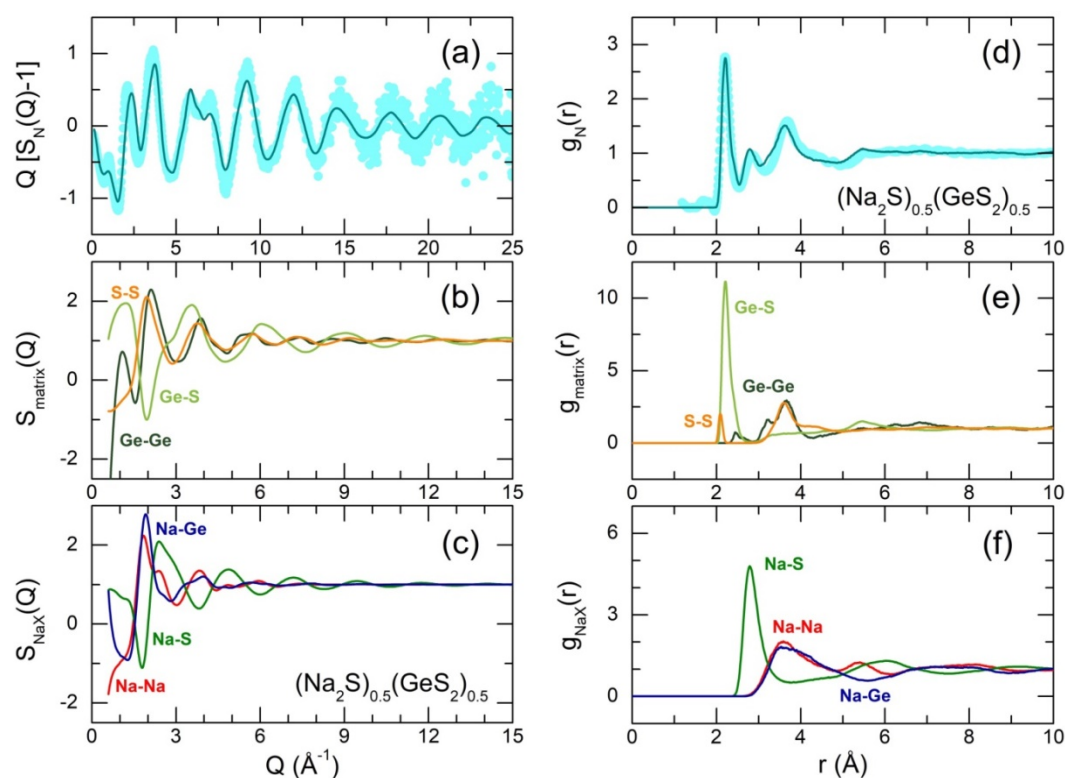


Figure 7. FPMD of equimolar $(\text{Na}_2\text{S})_{0.5}(\text{GeS}_2)_{0.5}$: (a) neutron interference function $Q[S_{\text{N}}(Q) - 1]$ (the solid line) plotted together with obtained experimental data (the light cyan circles); partial structure factors $S_{ij}(Q)$ for (b) Ge-Ge (dark green), Ge-S (light green), S-S (yellow), and (c) Na-S (green), Na-Na (red), and Na-Ge (dark blue) correlations; (d) FPMD (the solid line) and experimental (the light cyan circles) neutron pair-distribution functions $g_{\text{N}}(r)$; partial pair-distribution functions $g_{ij}(r)$ for (e) Ge-Ge, Ge-S, S-S, and (f) Na-S, Na-Na, and Na-Ge atomic pairs.

The partial structure factors $S_{ij}(Q)$ are shown in Figure 7b,c. We note that the main contribution to the FSDP comes from Ge-Ge and to some extent from Ge-S correlations while a large negative contribution is related to the Na-Ge partial structure factor. The FPMD partial pair-distribution functions $g_{ij}(r)$ are summarized in Figure 7e,f. As expected, the main first nearest neighbor peak essentially consists of Ge-S atomic pairs centered at 2.22 Å. The peak is strongly asymmetric consisting of short $\text{Ge}_{4\text{F}}\text{-S}$ and long $\text{Ge}_{3\text{F}}\text{-S}$ distances as in crystalline GeS_2 or sodium thiogermanates, $2.14 \leq r_{\text{Ge}_{4\text{F}}\text{-S}} \leq 2.26$ Å,^{39-41,70} and orthorhombic GeS , $r_{\text{Ge}_{3\text{F}}\text{-S}} = 2.443$ Å.⁸⁵ The statistical analysis of FPMD simulation boxes in thermal equilibrium at 300 K yields $\text{Ge}_{4\text{F}}\text{-S}$ and $\text{Ge}_{3\text{F}}\text{-S}$ distance distributions, Figure 8c, centered at 2.22 Å and 2.38 Å, respectively.

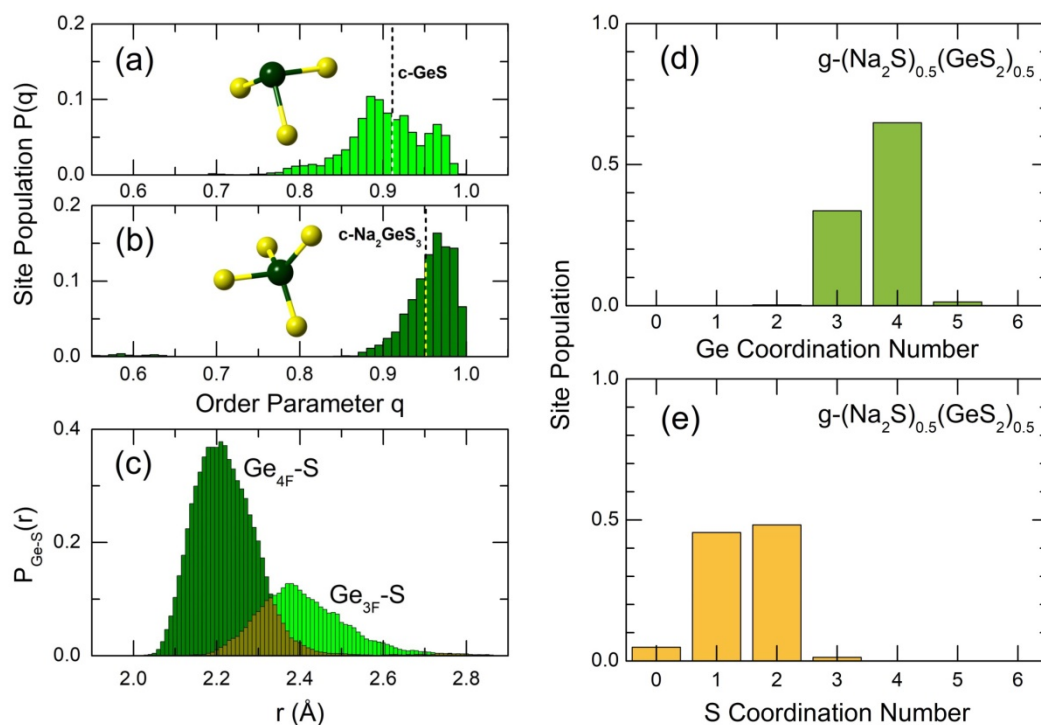


Figure 8. FPMD structural parameters for Ge-S subnetwork in glassy $(\text{Na}_2\text{S})_{0.5}(\text{GeS}_2)_{0.5}$: (a,b) orientational order parameter q and (c) Ge-S distance distributions for four-fold $\text{Ge}_{4\text{F}}$ and three-fold $\text{Ge}_{3\text{F}}$ germanium species; (d) germanium and (e) sulfur local coordination distributions. The q -parameters for crystalline GeS and Na_2GeS_3 are also shown.

We also note a small fraction of homopolar Ge-Ge bonds at 2.45 Å, seen in the diffraction and Raman experiments (Figure S6 and respective comments), and an S-S first neighbor peak at 2.10 Å. A weak amplitude of the S-S homopolar bonds makes impossible to detect them in a neutron scattering experiment, taking into account a small neutron coherent scattering length for sulfur ($\bar{b} = 2.847$ fm) compared to germanium (8.185 fm) and sodium (3.58 fm). Nevertheless, Raman spectroscopy of equimolar glassy $(\text{Na}_2\text{S})_{0.5}(\text{GeS}_2)_{0.5}$ shows the S-S stretching, Figure 4d, supported by DFT modeling with consistent S-S interatomic distances.

The FPMD partial coordination numbers are collected in Table 1, revealing a good agreement with the experimental values. In particular, the total germanium coordination was also found to be below four: $N_{\text{Ge-X}} = N_{\text{Ge-S}} + N_{\text{Ge-Ge}} = 3.58 + 0.09 = 3.67$. It means that the Ge-centered polyhedra contain both tetrahedral GeX_4 and trigonal GeX_3 entities. The Ge coordination distribution is shown in Figure 8d and reveals $\frac{2}{3}$ of tetrahedra and $\frac{1}{3}$ of pyramids with negligible population of under- and over-coordinated Ge-X units.

The tetrahedral shape of GeX_4 entities clearly shows the orientational order parameter q ,^{86,87} Figure 8a and b, extended beyond the tetrahedral geometry⁸⁸⁻⁹⁰

$$q = 1 - \frac{3}{8} \sum_{j=1}^{n-1} \sum_{k=j+1}^n \left(\cos \psi_{jk} + \frac{1}{3} \right)^2, \quad (5)$$

where ψ_{jk} is the X-Ge-X angle of a given GeX_n unit, see also Figure S9 and related more detailed comments. The non-tetrahedral fraction is negligible, 2.6%. Basically, the GeX_4 tetrahedra are slightly more distorted than those in monoclinic Na_2GeS_3 , confirmed also by the S-Ge_{4F}-S bond angle distribution $B_{\text{SGeS}}(\theta)$, Figure S10b. In contrast to tetrahedral germanium, the GeX_3 trigonal pyramids are highly distorted in comparison with orthorhombic GeS evidenced by $P(q)$, Figures 8a and S9a, and $B_{\text{SGeS}}(\theta)$, Figure S10a.

The partial sulfur local coordination, $N_{\text{S-X}} = N_{\text{S-Ge}} + N_{\text{S-S}} = 1.19 + 0.27 = 1.46$, is below two. In addition to usual bridging sulfur S(*b*), $N_{\text{S}(b)\text{-Ge}} = 2$, glassy $(\text{Na}_2\text{S})_{0.5}(\text{GeS}_2)_{0.5}$ contains a comparable fraction of terminal sulfur S(*t*), $N_{\text{S}(t)\text{-Ge}} = 1$, Figure 8e. Ideally, these two fractions should be identical for equimolar composition: $\text{Na}_2\text{S} + \text{GeS}_2 = \text{GeS}(t)_2\text{S}(b)_{2/2} + 2\text{Na}^+$. The simulated values are very close to these expectations. We should also note a non-negligible fraction of isolated sulfur, which does not have Ge nearest neighbors. We will discuss the role of these sulfur species later.

The Ge-Ge second neighbor correlations exhibit a bimodal shape, Figure 7e. The short Ge-Ge second neighbor distances at 3.19 Å are related to edge-sharing units, supported by the low- θ shoulder for $B_{\text{SGeS}}(\theta)$ and bimodal distributions of $B_{\text{GeSGe}}(\theta)$, Figure S10. The longer Ge-Ge correlations at 3.67 Å correspond to CS-tetrahedra/pyramids. The fraction of the ES-entities is lower in glassy $(\text{Na}_2\text{S})_{0.5}(\text{GeS}_2)_{0.5}$, $f_{\text{ES}} = 0.27$, compared to $f_{\text{ES}} = 0.49 \pm 0.05$ for g- GeS_2 (Table 1). The tetrahedral connectivity, reflected by Ge_{4F}-S-Ge_{4F} bond angles, is reminiscent of monoclinic HT- GeS_2 ,⁷⁰ Figure S10d, although both trigonal and tetrahedral connectivities are rather different in comparison with crystalline references.

Similar to $\text{Na}_2\text{S-As}_2\text{S}_3$ glasses,³⁰ the local sodium coordination is ill-defined. The $g_{\text{NaS}}(r)$ partial function, Figure 7f, exhibits a long high- r tail for the Na-S nearest neighbors overlapping with the second coordination sphere. As a result, the correct evaluation of the local sodium environment appears to be difficult. Fitting the $T_{\text{NaS}}(r)$ partial correlation function with multiple Gaussians, we can reproduce the asymmetric shape of the nearest neighbor peak, Figure 9a. Assuming the first two contributions are related to the Na-S nearest neighbors and more distant contributions correspond to the second coordination sphere, we obtain the Na-S local coordination number $N_{\text{Na-S}} = 4.12$. Taking the maximum Na-S distance in crystalline Na_2GeS_3 as a cutoff, one obtains $N_{\text{Na-S}} = 3.72$. Finally, taking a shallow minimum of $T_{\text{NaS}}(r)$ at 3.70 Å as a cutoff, the Na-S local coordination number appears to be 5.32. Averaging these values, our estimation of the local sodium coordination number is $N_{\text{Na-S}} = 4.5 \pm 0.5$. The sodium coordination distribution corresponding to this average value is shown in Figure 9b. As expected, the populations of 4-fold and 5-fold coordinated sodium sites are nearly identical. The distribution is symmetric with the less populated under- and over-coordinated sodium species.

The sodium environment is strongly distorted as evidenced by the $B_{\text{SNaS}}(\theta)$ bond angle distribution, Figure 9c. Roughly, the sodium local surroundings appear to be a broadened deformed version of sodium polyhedra in monoclinic Na_2GeS_3 and fcc Na_2S . The polyhedral

connectivity reflected by $B_{\text{NaSNa}}(\theta)$ is also rather similar to that in the above crystalline mixture although the Na-S-Na angles between $120^\circ \lesssim \theta \lesssim 150^\circ$ are missing in both Na_2GeS_3 and Na_2S .

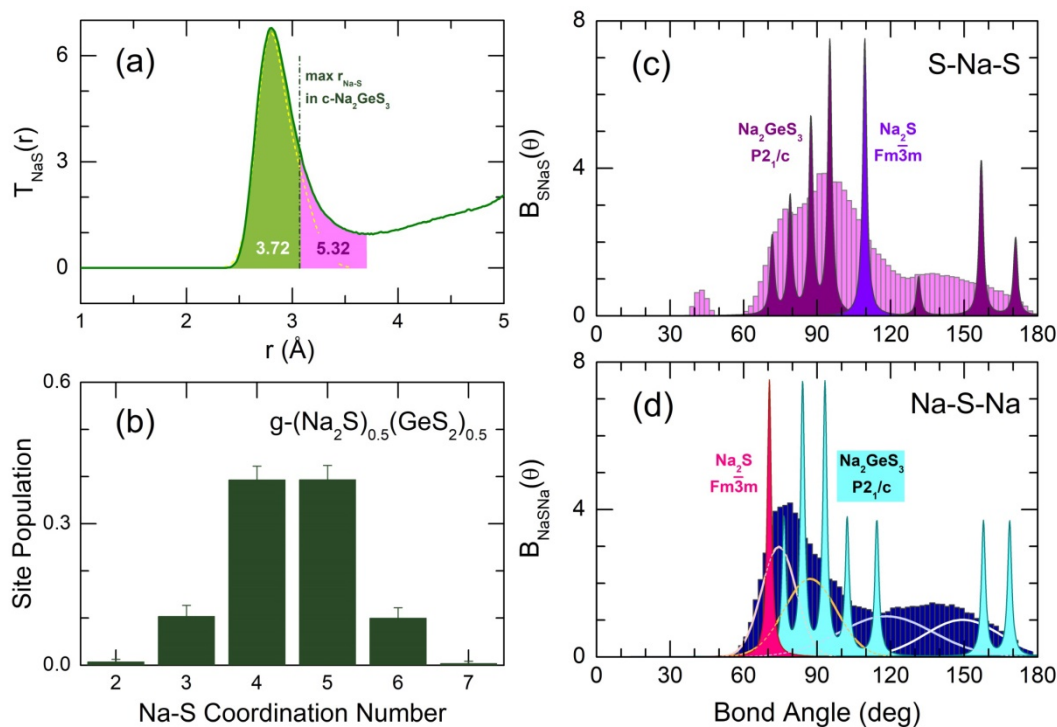


Figure 9. FPMD structural parameters for Na-S subnetwork in glassy $(\text{Na}_2\text{S})_{0.5}(\text{GeS}_2)_{0.5}$: (a) various approaches to determine sodium coordination environment; the yellow dashed line represents the sum of two Gaussian functions related to Na-S nearest neighbors, the black dash-dotted line shows the maximum Na-S distance in monoclinic Na_2GeS_3 ; (b) Na-S coordination distribution, $B(\theta)$ angular distributions for (c) S-Na-S and (d) Na-S-Na bond angles. The $B_{\text{SNaS}}(\theta)/B_{\text{NaSNa}}(\theta)$ functions for crystalline Na_2GeS_3 and Na_2S are also shown.

The connectivity analysis shows that 61% of Ge and S atoms are still forming a single connected Ge-S fragment in the simulation box. The remaining 39% represent either isolated S atoms or small oligomeric fragments, Figure S11. The obtained results are very different from crystalline Na_2GeS_3 , consisting of infinite corner-sharing chains $\text{CS}-[\text{GeS}(t)_2\text{S}(b)_{2/2}^-]_\infty$ held together by sodium cations.⁴⁰ The small oligomeric fragments represent isolated tetrahedra ISO- GeS_4 or trigonal pyramids ISO- GeS_3 , corner- CS- Ge_2S_5 and edge-sharing ES- Ge_2S_6 dimers or mixed oligomeric ES/CS-chains, all connected by sodium. The single large connected fragment is roughly a complicated chain consisting of CS- and ES-segments, including also small rings and homopolar S-S and Ge-Ge dimers. A chain-like character of the connected fragments confirms a clear majority ($\approx 4/5$) of corner-sharing polyhedra, CS- GeX_4 and CS- GeX_3 , which are predominantly forming chains, $N_{\text{Ge-Ge}}^{\text{CS}} = 1.82$. Figure S12 and related comments reveal that trigonal Ge is distributed rather randomly in the glass network with the average $\text{Ge}_{3\text{F}}\text{-Ge}_{3\text{F}}$ separation distance of 5.7 ± 0.5 Å. In contrast, the $\text{Ge}_{4\text{F}}$ -centered units are forming complex n -membered chains, $n \leq 35$.

The DFT vibrational signatures of typical Na-Ge-S clusters observed in FPMD appear to be consistent with experimental Raman spectra of sodium thiogermanate glasses, Figure S8. In particular, a lower frequency symmetric $\text{Ge}_{3\text{F}}\text{-S}$ breathing explains the red shift of the broad

unresolved A_1 glassy breathing mode over the spectral range $343 \leq \omega_{A_1} \leq 328 \text{ cm}^{-1}$ (Figure 2b) with corresponding increase of the average Ge-S interatomic distances (Table 1).

The derived ring statistics in comparison with that in glassy GeS_2 is shown in Figure 10. We note an enormous difference in size, $(p+q)$, and population $R_c(p+q)^{67}$ of Ge_pS_q rings between the two glasses, revealing a complete disappearance of the intermediate range order typical for g- GeS_2 . One should however mention that this is not a simple network fragmentation, since 61% of Ge and S are still connected but a profound transformation of the original GeS_2 host with sodium sulfide additions.

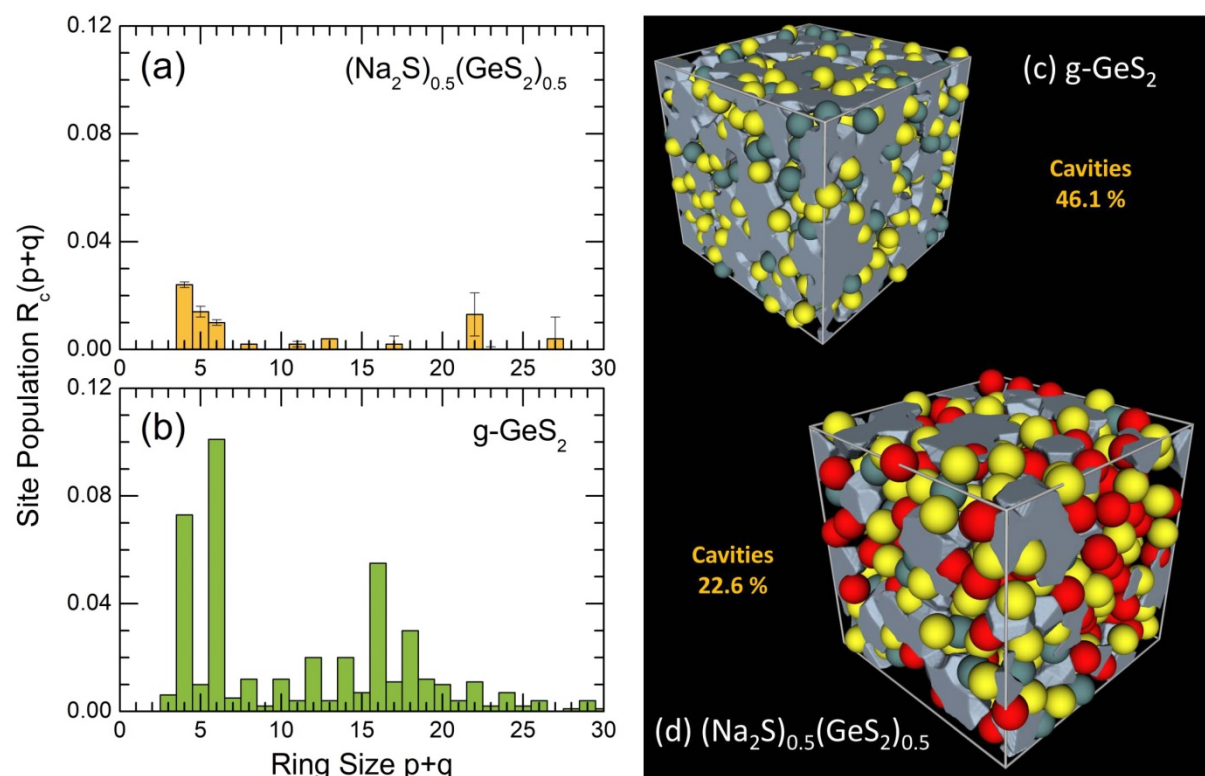


Figure 10. Rings and voids: Ge_pS_q ring statistics in (a) equimolar $(\text{Na}_2\text{S})_{0.5}(\text{GeS}_2)_{0.5}$ and (b) glassy GeS_2 ; microscopic cavities in (c) vitreous GeS_2 and (d) glassy $(\text{Na}_2\text{S})_{0.5}(\text{GeS}_2)_{0.5}$.

This transformation can also be seen differently, analyzing the microscopic voids and cavities. Using the pyMolDyn code⁶⁹ and the Dirichlet-Voronoi tessellation, we have found a significant decrease of the total volume of cavities V_c , normalized to the volume of the simulation box, $0 \leq V_c \leq 1$, in case of the sodium thiogermanate glass, Figure 10. Glassy GeS_2 has 46.1% of voids, that is, nearly one half of the glass volume is unoccupied. Alloying with sodium decreases significantly the cavities and voids, and the total volume of voids drops to 22.6%. It could be interpreted as the sodium species are located in previously empty spaces within the glass network. More importantly, a two-fold difference in V_c indicates a more dense packing of sodium thiogermanate glasses also reflected by the increased amplitude of the principle peak PP in the neutron structure factor for $\text{Na}_2\text{S-GeS}_2$ glasses, Figure 5.

The FPMD sodium local dynamics can be compared with long-range sodium diffusion calculated from the experimental ionic conductivity σ_i using the Nernst-Einstein relation,

$$D_{\sigma} = \frac{k_{\text{B}}T}{c_i(Ze)^2} \sigma_i, \quad (6)$$

where D_{σ} is the diffusion (conductivity) coefficient, c_i the atomic sodium concentration, Ze the electric charge of the carrier ion, k_{B} and T have their usual meaning. The sodium mean square displacements $\langle r_{\text{Na}}^2(t) \rangle$ as a function of time t are defined as

$$\langle r_{\text{Na}}^2(t) \rangle = \left\langle \frac{1}{N_i} \left\{ \sum_{i=1}^{N_i} [r_i(t) - r_i(0)]^2 \right\} \right\rangle, \quad (7)$$

where $r_i(0)$ and $r_i(t)$ are the positions of sodium atom i for the initial time and time t , respectively, N_i the total number of sodium in the simulation box, and the angle brackets represent the average over initial times. The $\langle r_{\text{Na}}^2(t) \rangle$ values are shown in Figure 11 on linear and log-log scales for the highest FPMD temperature of 600 K, corresponding to supercooled liquid above $T_{\text{g}} = 498 \pm 2$ K.

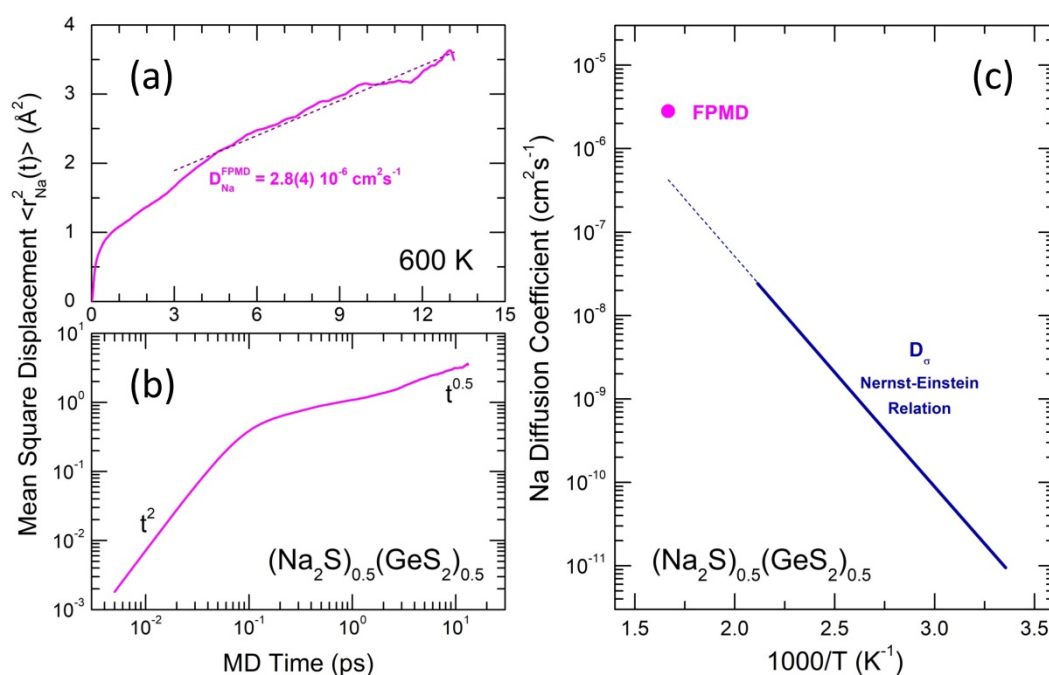


Figure 11. FPMD atomic dynamics in equimolar $(\text{Na}_2\text{S})_{0.5}(\text{GeS}_2)_{0.5}$; sodium mean square displacements at 600 K on (a) linear and (b) log-log scales, (c) the derived sodium diffusion coefficients $D_{\text{Na}}^{\text{FPMD}}(\text{eff})$ and D_{σ} . See text for further details.

As expected, the ballistic regime is observed at low $t \lesssim 30$ fs, Figure 11b, revealing a slope $s = 2$ on a log-log scale⁹¹

$$\langle r_{\text{Na}}^2(t) \rangle \propto \left(\frac{k_{\text{B}}T}{m_{\text{Na}}} \right) t^2, \quad (8)$$

where m_{Na} is the sodium atomic mass, followed by transient phenomena and the beginning of diffusive motion for the last 10 ps. Nevertheless, a long-range Brownian diffusion process, characterized by a linear function of time,⁹²

$$\langle r_{\text{Na}}^2(t) \rangle \propto D_{\text{Na}}^{\text{FPMD}} t^1, \quad (9)$$

where $D_{\text{Na}}^{\text{FPMD}}$ is the average sodium diffusion coefficient, has not been observed over the used temperature – time domain, mostly limiting the sodium mobility to localized displacements. A typical evolution of the atomic dynamics over a wide temperature – time range is given in Figure S13.⁹³ The derived effective sodium diffusion coefficient $D_{\text{Na}}^{\text{FPMD}}(\text{eff})$

$$D_{\text{Na}}^{\text{FPMD}}(\text{eff}) = \frac{1}{6} \lim_{t \rightarrow t_{\text{max}}} \frac{\partial \langle r_{\text{Na}}^2(t) \rangle}{\partial t}, \quad (10)$$

where the time domain is restricted by the last 10 ps, appears to be overestimated in comparison with long-range sodium migration, Figure 11c. This is not surprising since cation mobility is faster on a shorter spatial and time scale, see for example,⁹⁴ and references therein. It should also be noted that the observed difference, $D_{\text{Na}}^{\text{FPMD}}(\text{eff})/D_{\sigma} = 7 \pm 2$, might be lower, while D_{σ} corresponds to a solid glass, and $D_{\text{Na}}^{\text{FPMD}}(\text{eff})$ to a supercooled liquid. Further discussion on sodium atomic motion will be given below.

3.4. Isolated Sulfur and Preferential Diffusion Pathways. As emphasized in Introduction, a special attention should be paid to isolated sulfur species S_{iso} , that is, the sulfur atoms without direct connections to germanium. The isolated sulfur species are connected only to sodium, and the average Na/ S_{iso} stoichiometry is approximately $[\text{Na}]/[S_{\text{iso}}] \approx 2$. In contrast to the $(\text{Na}_2\text{S})_{0.3}(\text{As}_2\text{S}_3)_{0.7}$ glass with a modest S_{iso} fraction of 6.2%,³⁰ equimolar $(\text{Na}_2\text{S})_{0.5}(\text{GeS}_2)_{0.5}$ exhibits $S_{\text{iso}}/S_{\text{tot}} = 0.169$, Figure 12. The derived fraction is still lower than that in superionic $\text{Ag}_2\text{S}-\text{As}_2\text{S}_3$ or $\text{Ag}_2\text{S}-\text{GeS}_2$ glasses, $0.18 \leq S_{\text{iso}}/S_{\text{tot}} \leq 0.21$,²⁹ and even is less significant than the S_{iso} fraction in the same glass reported previously, 23.5%.³⁶ However, the obtained results using identical GGA/PBE0 simulation approach appear to be systematic, and the ratio $\sigma_{\text{Ag}}/\sigma_{\text{Na}} \approx 1000$ for the silver and sodium equimolar thiogermanate glasses, Figure 1b, is consistent with the difference in $S_{\text{iso}}/S_{\text{tot}}$.

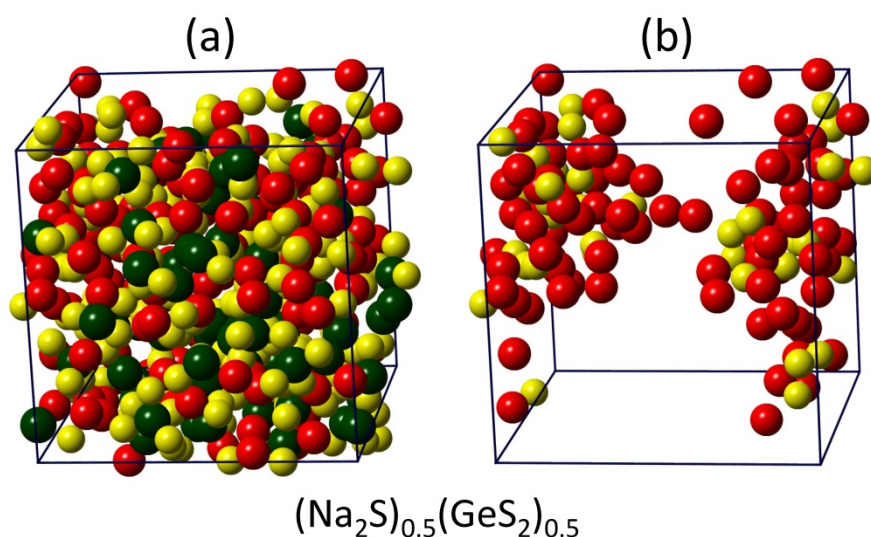


Figure 12. Isolated sulfur S_{iso} in glassy $(\text{Na}_2\text{S})_{0.5}(\text{GeS}_2)_{0.5}$: (a) the entire FPMD simulation box containing 450 atoms (150 Na, 75 Ge and 225 S), (b) isolated sulfur species with connected sodium atoms.

The isolated sulfur species with connected sodium are located in a close proximity to each other forming preferential conduction pathways. These pathways are still not as efficient as in superionic silver glasses but they are drastically different compared to the S_{iso} distribution in

low-conducting $(\text{Na}_2\text{S})_{0.3}(\text{As}_2\text{S}_3)_{0.7}$,³⁰ where the average distance between Na-S_{iso} units is 6.7 Å for more than 50% of the sodium species involved. Taking into account the Na/S_{iso} stoichiometry, 58% of sodium are connected to S_{iso} species in $\text{g-}(\text{Na}_2\text{S})_{0.5}(\text{GeS}_2)_{0.5}$, indicating a predominant role of Na^+ ion transport via these diffusion channels. In superionic silver ternaries, the fraction of Ag-S_{iso} associates is even higher: 67% for $(\text{Ag}_2\text{S})_{0.6}(\text{As}_2\text{S}_3)_{0.4}$ and 74% for $(\text{Ag}_2\text{S})_{0.45}(\text{GeS}_2)_{0.45}$. We should also note an astonishing contrast in σ_i between glassy $(\text{Na}_2\text{S})_{0.5}(\text{GeS}_2)_{0.5}$ and monoclinic Na_2GeS_3 , Figure 1b. The crystalline counterpart without isolated sulfur exhibits the room-temperature conductivity by 8 orders of magnitude lower.

The question arises whether a remarkable $\sigma_{\text{Ag}}/\sigma_{\text{Na}}$ difference both for $(\text{M}_2\text{S})_{0.5}(\text{GeS}_2)_{0.5}$ (3 orders of magnitude, Figure 1b) and $(\text{M}_2\text{S})_{0.3}(\text{As}_2\text{S}_3)_{0.7}$ (4.5 orders of magnitude, Figure S1) glasses may be related to intrinsically low sodium ion mobility in sulfide systems compared to fast Ag^+ ions. The answer is given in Figure 13a, revealing ^{22}Na and $^{110\text{m}}\text{Ag}$ tracer diffusion coefficients in diluted thioarsenate glasses of identical stoichiometry $(\text{M}_2\text{S})_{0.01}(\text{As}_2\text{S}_3)_{0.99}$, in which no preferential conduction pathways are yet formed.^{27,29} Sodium diffusion was found to be slightly lower, $D_{\text{Ag}}/D_{\text{Na}} = 2.4 \pm 0.6$ at 448 K, but incomparable with 3 or 4.5 orders of magnitude difference in cation-rich vitreous systems. In other words, the isolated sulfur fraction seems to be an appropriate descriptor of fast ion transport in glasses, at least, for sodium and silver vitreous sulfides, Figure 13b.

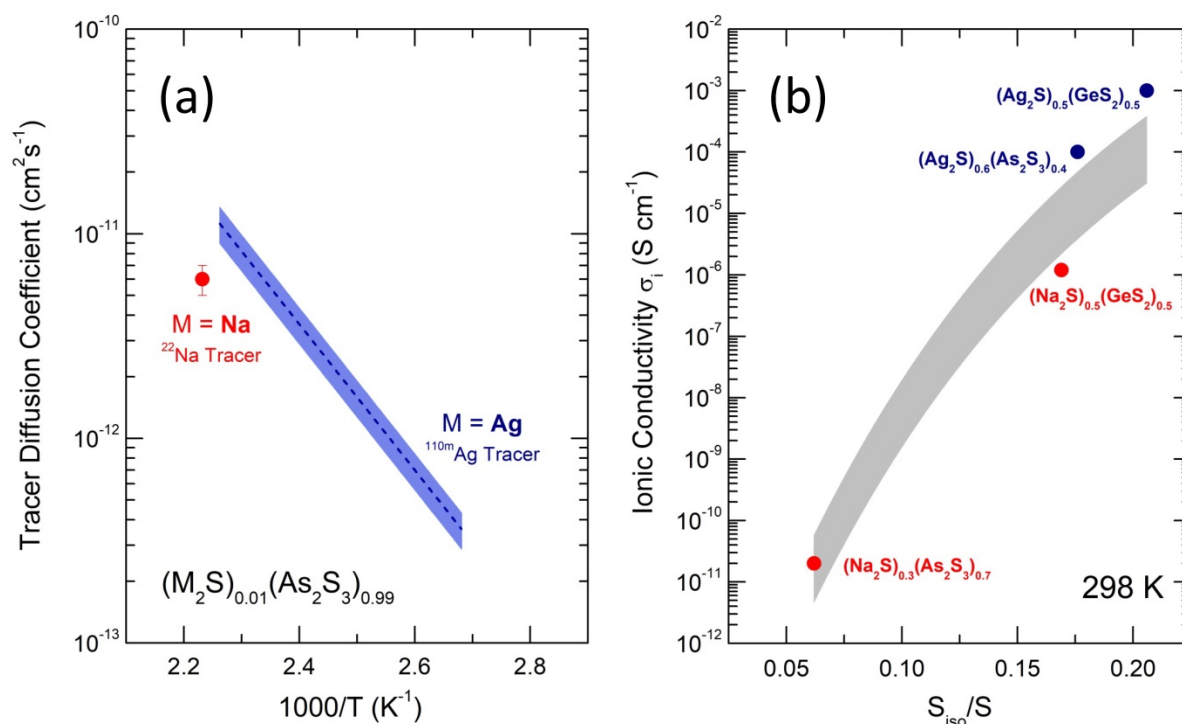


Figure 13. Ion transport properties in silver and sodium vitreous sulfides: (a) ^{22}Na (this work) and $^{110\text{m}}\text{Ag}$ (Ref.²⁶) tracer diffusion coefficients in glassy $(\text{M}_2\text{S})_{0.01}(\text{As}_2\text{S}_3)_{0.99}$; (b) room-temperature ionic conductivity σ_{298} for silver and sodium ternary sulfides as a function of isolated sulfur fraction $S_{\text{iso}}/S_{\text{tot}}$.

As expected, sodium atomic dynamics is heterogeneous⁹⁵ in vitreous $(\text{Na}_2\text{S})_{0.5}(\text{GeS}_2)_{0.5}$, Figure 14b,c. Two-thirds of the sodium mean-square displacements (MSD) at 600 K are below 2 Å², and only 8.7% are characterized by $\langle r_{\text{Na}}^2(t) \rangle \geq 10$ Å², that is, may be considered as a long-range Brownian motion. The Na trajectories over 13 ps are shown in Figure 14a using the [100] projection of the FPMD simulation box. We note a non-random sodium dynamical distribution,

where dark red domains reflect more dense mobile Na population. A majority of these domains are decorated by isolated sulfur, Figure 14a'.

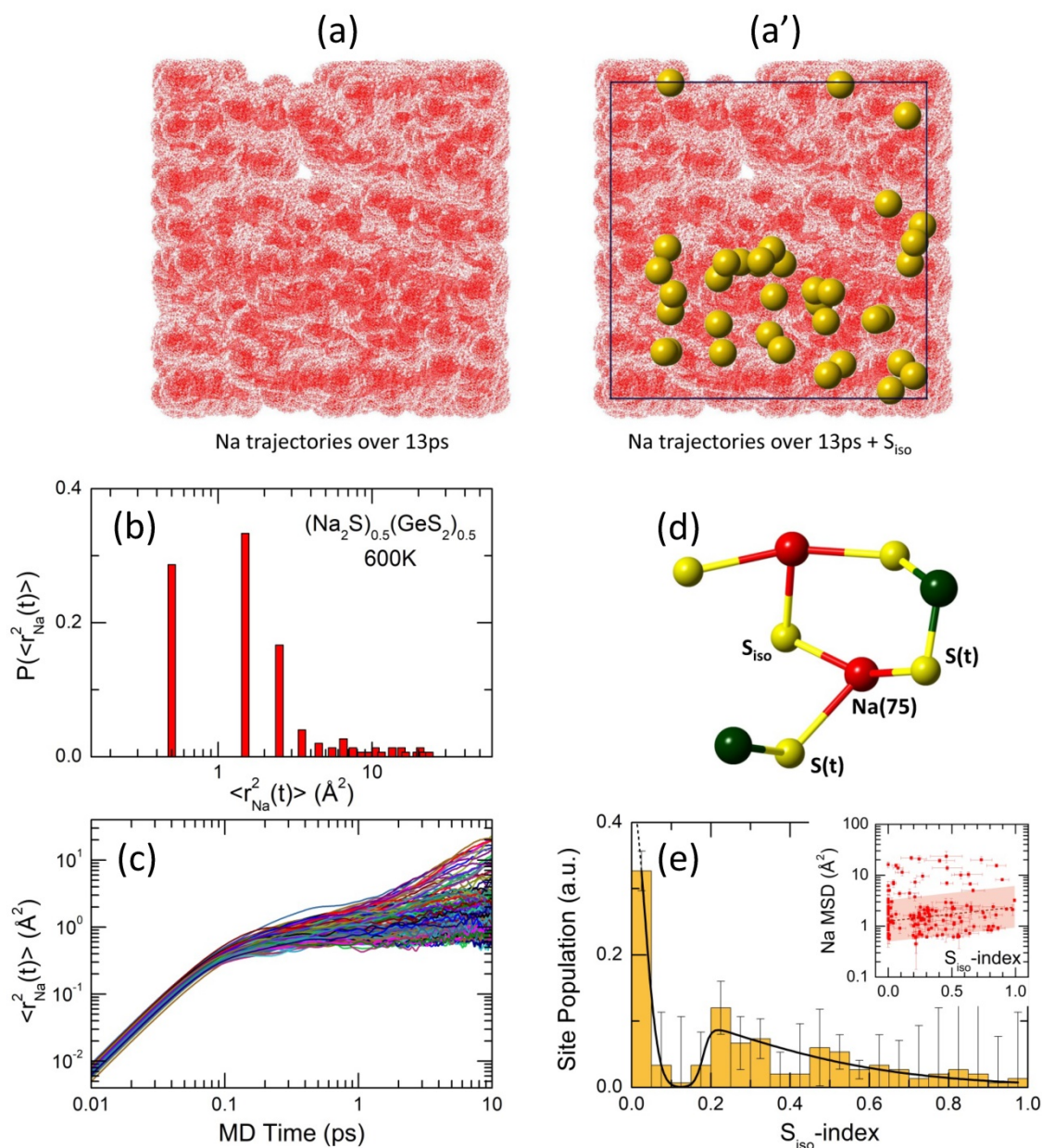


Figure 14. Temporal and spatial sodium atomic dynamics in $(\text{Na}_2\text{S})_{0.5}(\text{GeS}_2)_{0.5}$ at 600 K. (a,a') Na trajectories over 13 ps using the [100] projection of the FPMD simulation box; heterogeneous sodium dynamics: (b) probability distribution function $P(\langle r_{\text{Na}}^2(t) \rangle)$ of Na MSD for $t = 10$ ps, (c) individual Na MSD as a function of time; (d) schematic definition of isolated sulfur index, (e) distribution of time-averaged S_{izo} -index for sodium species at 600 K, the inset shows the sodium MSD as a function of S_{izo} -index. See text for further details.

A semi-quantitative estimation of a possible correlation between the mobile sodium environment and $\langle r_{\text{Na}}^2(t) \rangle$ may be given using a time-averaged S_{izo} -index, that is, the fraction of S_{izo} nearest neighbors in the sodium environment over a particular Na trajectory. Figure 14d shows incomplete, for simplicity, local environment of Na(75), one of the 150 sodium species present in the simulation box for a particular time t_i . Between three shown sulfur nearest neighbors, two belong to terminal sulfur $S(t)$ and one is S_{izo} . Consequently, the S_{izo} -index is

$i_{S_{iso}}(t_i) = 1/3$. The bimodal distribution of time-averaged $\langle i_{S_{iso}}(t) \rangle$ for sodium species is given in Figure 14e. About 40% of sodium over the entire trajectories is mostly surrounded by terminal sulfur, $\langle i_{S_{iso}}(t) \rangle \lesssim 0.1$. The remaining distribution is asymmetric with a maximum at $\langle i_{S_{iso}}(t) \rangle \approx 0.25$ and a long tail toward pure S_{iso} environment, $\langle i_{S_{iso}}(t) \rangle = 1$. Nevertheless, the S_{iso} -rich population, $\langle i_{S_{iso}}(t) \rangle > 0.5$, represents only one-quarter. The inset in Figure 14e shows the average sodium MSDs over the last 5 ps as a function of time-averaged S_{iso} -index. In spite of a strong scatter of the data points and a large temporal variability of $\langle i_{S_{iso}}(t) \rangle$, a distinct correlation reveals an increase of the sodium mobility for S_{iso} -rich environment, roughly by a factor of two.

In this context, additional information yields comparison of Na-Na partial pair-distribution functions $g_{NaNa}(r)$ for equimolar $(Na_2S)_{0.5}(GeS_2)_{0.5}$ and crystalline references Na_2GeS_3 and Na_2S , Figure 15. For sodium sulfide, both room-temperature $g_{NaNa}(r)$ is given and that at 1100 K. A drastic difference between the Na-Na partials in low-conducting and superionic Na_2S appears to be consistent with a dramatic change in σ_i and D_{Na} of 10 orders of magnitude for σ_i , Figure 1.

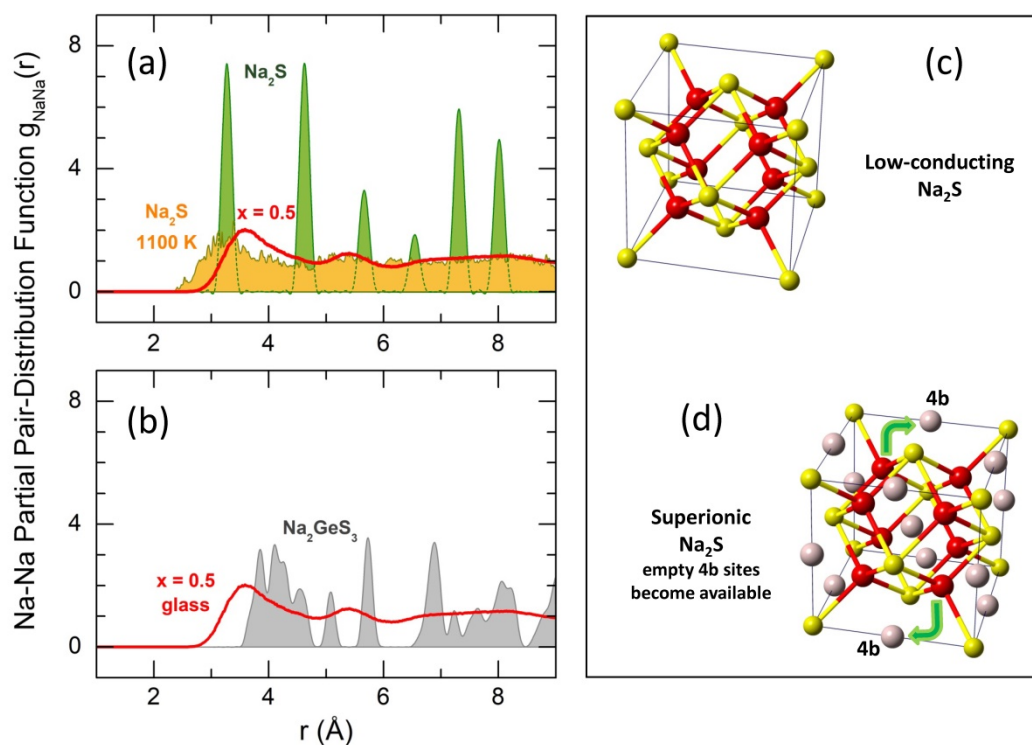


Figure 15. Partial Na-Na pair-distribution functions $g_{NaNa}(r)$ in glassy $(Na_2S)_{0.5}(GeS_2)_{0.5}$ (the red solid line) and crystalline references: (a) Na_2S at room-temperature (highlighted in green) and 1100 K (highlighted in yellow), and (b) Na_2GeS_3 (highlighted in light grey). The room temperature crystalline $g_{NaNa}(r)$ were calculated from the cif files using the XTAL program.⁹⁶ Preliminary FPMD results are used for Na_2S at 1100 K. Face-centered cubic unit cell for (c) low-conducting and (d) superionic Na_2S . At high temperatures, $T \gtrsim 1000$ K, empty 4b positions (highlighted in light red) become available for sodium, opening up fast diffusion pathways.

The onset of type-II superionic transition in Li_2S and Na_2S , Figure 1, is associated with expected availability of previously empty 4b sites in the fcc lattice for alkalis²⁰ opening up efficient diffusion pathways for long-range Na^+ migration, Figure 15d. The $g_{NaNa}(r)$ broadening at 1100 K reflects this trend, especially at low r , since the partial occupancy of 4b sites reveals Na-Na

1
2
3 correlations centered at $r = 2.84 \text{ \AA}$. We note a striking similarity between the Na-Na partials in
4 equimolar $(\text{Na}_2\text{S})_{0.5}(\text{GeS}_2)_{0.5}$ and superionic Na_2S , Figure 15a, coherent with much higher σ_i and
5 D_{Na} for glassy sodium thiogermanates and thiogallates at ambient temperatures in comparison
6 with low-conducting Na_2S and Na_2GeS_3 , Figure 1. This difference is certainly related to the
7 existence of percolating diffusion pathways based on S_{iso} in sodium sulfide glasses.
8
9

10 The next question is what factors control the $S_{\text{iso}}/S_{\text{tot}}$ fraction? Basically, the first variable seems
11 to be the cation content x . Our FPMD simulations of sodium and silver ternary sulfides show
12 that 60 to 67% of glassy structural motifs are consistent with equilibrium phase diagrams and
13 crystalline motifs yet remaining disordered. Although the crystalline stoichiometry limits are
14 violated in glasses, the basic composition trend persists, and $S_{\text{iso}}/S_{\text{tot}}$ increases with x . The
15 crystalline stoichiometry limits depend on the local coordination of the glass-former, and the S_{iso}
16 species appear earlier in systems with four-fold coordinated Ge than in those with trigonal As.
17 An easy way to form the homopolar bonds can also be beneficial. Taking into account the
18 energies of homopolar and heteropolar bonds As-As, Ge-Ge, S-S, As-S and Ge-S, the As-As
19 homopolar bonds should be formed more easily since $(E_{\text{A-A}} + E_{\text{S-S}})/2E_{\text{A-S}} = 0.94$ for $A = \text{As}$ and
20 0.87 for $A = \text{Ge}$.⁹⁷ On the other hand, the chemical disorder in glassy GeS_2 and As_2S_3 is roughly
21 similar, $[\text{As-As}]/([\text{As-As}] + [\text{As-S}])$ or $[\text{Ge-Ge}]/([\text{Ge-Ge}] + [\text{Ge-S}]) = 1-3 \%$.^{82,97} Finally, a structural
22 instability in glasses can also be noted. In particular, the germanium disulfide glassy systems
23 exhibit a partial disproportionation: $\text{GeS}_2 \rightarrow \text{GeS} + \text{S}$, and trigonal GeS-related structural motifs
24 appear instead of GeS_4 tetrahedra, accompanied by additional sulfur, transforming into S_{iso} . This
25 instability was observed in Ge-rich binaries,⁸² silver²⁹ and sodium thiogermanate glasses,
26 Sections 3.2 and 3.3. An extreme case of tetrahedral metastability shows GeTe_2 in crystalline^{98,99}
27 and glassy⁸⁹ states.
28
29
30
31
32

33 The equilibrium phase diagrams and glassy $S_{\text{iso}}/S_{\text{tot}}$ are also correlated differently. The Ag_2S -
34 GeS_2 ternary system exhibits superionic argyrodite Ag_8GeS_6 , which contains $\frac{1}{3}$ of S_{iso} . The silver-
35 rich thioarsenate counterpart is just Ag_3AsS_3 , the composition limit of emerging S_{iso} . Broadly
36 speaking, the isolated sulfur species are more favorable energetically in silver thiogermanates
37 than in silver thioarsenates. These observations are consistent with glassy $S_{\text{iso}}/S_{\text{tot}}$ and
38 composition trends in ionic conductivity and tracer diffusion, Figures 1 and 13.
39
40
41
42
43

44 4. CONCLUSIONS

45 Pulsed neutron diffraction and Raman spectroscopy supported by first-principles simulations
46 were used in decoding structural and chemical roots of fast ion transport in vitreous $\text{Na}_2\text{S-GeS}_2$
47 and comparing with its silver counterparts, as well as sodium and silver thioarsenates. It was
48 found that 60 to 67% of glassy structural motifs follow the equilibrium phase diagrams and
49 crystalline motifs, remaining strongly disordered; however, the stoichiometry limits are violated
50 leading additionally to a topological disorder and unexpected chemical and structural features.
51 In particular, the preferential diffusion pathways in these systems are related to isolated sulfur
52 S_{iso} , that is, the sulfur species surrounded exclusively by mobile cations with a typical
53 stoichiometry $M/S_{\text{iso}} \approx 2$. The $S_{\text{iso}}/S_{\text{tot}}$ fraction appears to be a reliable descriptor of fast ion
54 transport in glassy systems over a wide range of ionic conductivities and cation diffusivities.
55 The S_{iso} fraction increases with mobile cation content x , tetrahedral coordination of the network
56 former and, in case of thiogermanate systems, with germanium disulfide metastability and
57
58
59
60

1
2
3 partial disproportionation, $\text{GeS}_2 \rightarrow \text{GeS} + \text{S}$, leading to formation of additional sulfur,
4 transforming into S_{iso} . A research strategy enabling to achieve extended and interconnected
5 pathways based on isolated sulfur would lead to sodium glassy electrolytes with superior
6 transport properties.
7
8
9

10 ASSOCIATED CONTENT

11 Supporting Information

12
13 The Supporting Information is available free of charge at <https://pubs.acs.org/doi/10.1021/>
14
15

16
17 Ionic conductivity of vitreous sodium and silver thioarsenates, sodium thiogermanate
18 and thiogallate; typical gamma-spectrum of ^{22}Na tracer; typical ^{22}Na tracer diffusion
19 profile; Ge-S(t) stretching as a function of x in the $(\text{Na}_2\text{S})_x(\text{GeS}_2)_{1-x}$ glasses; integration
20 procedure for Raman spectra of $(\text{Na}_2\text{S})_x(\text{GeS}_2)_{1-x}$ glasses; Ge-Ge and S-S stretching in
21 Raman spectra of $(\text{Na}_2\text{S})_x(\text{GeS}_2)_{1-x}$ glasses; experimental and DFT Raman spectra of
22 Na-S and S-S stretching in glasses; DFT Raman spectra of size-limited Ge-S and Na-Ge-S
23 clusters; orientational order parameter q ; bond angle distributions for trigonal and
24 tetrahedral Ge species; small fragments forming a disconnected Ge-S subnetwork;
25 connectivity of $\text{Ge}_{3\text{F-S}}$ and $\text{Ge}_{4\text{F-S}}$ subsets; gallium mean-square displacements in GaS at
26 1000 K; optimized geometry of DFT clusters (PDF)
27
28
29
30
31
32

33 AUTHOR INFORMATION

34 Corresponding Author

35
36
37 **Eugene Bychkov** – *Laboratoire de Physico-Chimie de l'Atmosphère, Université du Littoral Côte*
38 *d'Opale, 59140 Dunkerque, France; orcid.org/0000-0002-3292-1205; Phone: +33 328*
39 *658250; Email: Eugene.Bychkov@univ-littoral.fr; Fax: +33 328 658244*
40
41

42 Authors

43
44 **Mohammad Kassem** – *Laboratoire de Physico-Chimie de l'Atmosphère, Université du Littoral*
45 *Côte d'Opale, 59140 Dunkerque, France; orcid.org/0000-0003-0512-0004*
46

47 **Tinehinane Bounazef** – *Laboratoire de Physico-Chimie de l'Atmosphère, Université du Littoral*
48 *Côte d'Opale, 59140 Dunkerque, France*
49

50
51 **Anton Sokolov** – *Laboratoire de Physico-Chimie de l'Atmosphère, Université du Littoral Côte*
52 *d'Opale, 59140 Dunkerque, France*
53

54 **Maria Bokova** – *Laboratoire de Physico-Chimie de l'Atmosphère, Université du Littoral Côte*
55 *d'Opale, 59140 Dunkerque, France*
56

57 **Daniele Fontanari** – *Laboratoire de Physico-Chimie de l'Atmosphère, Université du Littoral Côte*
58 *d'Opale, 59140 Dunkerque, France*
59
60

1
2
3 **Alex C. Hannon** – *ISIS Facility, Rutherford Appleton Laboratory, Didcot OX11 0QX, U.K.;*
4 *orcid.org/0000-0001-5914-1295*
5

6 **Igor Alekseev** – *Laboratoire de Physico-Chimie de l'Atmosphère, Université du Littoral Côte*
7 *d'Opale, 59140 Dunkerque, France; on leave from V. G. Khlopin Radium Institute, 194021 St.*
8 *Petersburg, Russia*
9

10 11 12 13 **Notes**

14
15 The authors declare no competing financial interest.
16
17

18 19 **ACKNOWLEDGMENTS**

20
21 This work was supported by the Région Hauts de France and the Ministère de l'Enseignement
22 Supérieur et de la Recherche (CPER Climibio) as well as by the European Fund for Regional
23 Economic Development. Work at the ISIS spallation neutron source (Rutherford Appleton
24 Laboratory) was performed within Proposal RB1820299 supported by the U.K. Science and
25 Technology Facilities Council. The FPMD simulations were carried out using the CALCULCO
26 computing platform, supported by SCoSI/ULCO (Service Commun du Système d'Information de
27 l'Université du Littoral Côte d'Opale). This work was also granted access to the HPC resources of
28 IDRIS under Allocations 2021-A0110910639 made by GENCI (Grand Equipement National de
29 Calcul Intensif).
30
31
32
33
34
35
36
37
38
39
40
41
42
43
44
45
46
47
48
49
50
51
52
53
54
55
56
57
58
59
60

REFERENCES

- (1) Famprakis, T.; Canepa, P.; Dawson, J. A.; Islam, M. S.; Masquelier, C. Fundamentals of Inorganic Solid-State Electrolytes for Batteries. *Nat. Mater.* **2019**, *18*, 1278–1291.
- (2) Zhang, S.; Yao, Y.; Yu, Y. Frontiers for Room-Temperature Sodium–Sulfur Batteries. *ACS Energy Lett.* **2021**, *6*, 529–536.
- (3) Doeff, M. M.; Clément, R. J.; Canepa, P. Solid Electrolytes in the Spotlight. *Chem. Mater.* **2022**, *34*, 463–467
- (4) Hayashi, A.; Noi, K.; Sakuda, A.; Tatsumisago, M. Superionic Glass-Ceramic Electrolytes for Room-Temperature Rechargeable Sodium Batteries. *Nat. Commun.* **2012**, *3*, 856–861.
- (5) Bo, S.-H.; Wang, Y.; Kim, J. C.; Richards, W. D.; Ceder, G. Computational and Experimental Investigations of Na-Ion Conduction in Cubic Na₃PSe₄. *Chem. Mater.* **2016**, *28*, 252–258.
- (6) Richards, W. D.; Tsujimura, T.; Miara, L. J.; Wang, Y.; Kim, J. C.; Ong, S. P.; Uechi, I.; Suzuki, N.; Ceder, G. Design and Synthesis of the Superionic Conductor Na₁₀SnP₂S₁₂. *Nat. Commun.* **2016**, *7*, 11009.
- (7) Kim, T. W.; Park, K. H.; Choi, Y. E.; Lee, J. Y.; Jung, Y. S. Aqueous-Solution Synthesis of Na₃SbS₄ Solid Electrolytes for All-Solid-State Na-Ion Batteries. *J. Mater. Chem. A* **2018**, *6*, 840–844.
- (8) Duchardt, M.; Ruschewitz, U.; Adams, S.; Dehnen, S.; Roling, B. Vacancy-Controlled Na⁺ Superionic Conduction in Na₁₁Sn₂PS₁₂. *Angew. Chem. Int. Ed.* **2018**, *57*, 1351–1355.
- (9) Ramos, E. P.; Zhang, Z.; Assoud, A.; Kaup, K.; Lalère, F.; Nazar, L. F. Correlating Ion Mobility and Single Crystal Structure in Sodium-Ion Chalcogenide-Based Solid State Fast Ion Conductors: Na₁₁Sn₂PnS₁₂ (Pn = Sb, P), *Chem. Mater.* **2018**, *30*, 7413–7417.
- (10) Hayashi, A.; Masuzawa, N.; Yubuchi, S.; Tsuji, F.; Hotehama, C.; Sakuda, A.; Tatsumisago, M. A Sodium-Ion Sulfide Solid Electrolyte with Unprecedented Conductivity at Room Temperature. *Nat. Commun.* **2019**, *10*, 5266.
- (11) Till P.; Agne, M. T.; Kraft, M. A.; Courty, M.; Famprakis, T.; Ghidui, M.; Krauskopf, T.; Masquelier, C.; Zeier, W. G. Two-Dimensional Substitution Series Na₃P_{1-x}Sb_xS_{4-y}Se_y: Beyond Static Description of Structural Bottlenecks for Na⁺ Transport. *Chem. Mater.* **2022**, *34*, 2410–2421.
- (12) Weber, D. A.; Senyshyn, A.; Weldert, K. S.; Wenzel, S.; Zhang, W.; Kaiser, B.; Berendts, S.; Janek, J.; Zeier, W. G. Structural Insights and 3D Diffusion Pathways within the Lithium Superionic Conductor Li₁₀GeP₂S₁₂. *Chem. Mater.* **2016**, *28*, 5905–5915.
- (13) Zhang, L.; Zhang, D.; Yang, K.; Yan, X.; Wang, L.; Mi, J.; Xu, B.; Li, Y. Vacancy-Contained Tetragonal Na₃SbS₄ Superionic Conductor, *Adv. Sci.* **2016**, *3*, 1600089.
- (14) Famprakis, T.; Bouyanfif, H.; Canepa, P.; Zbiri, M.; Dawson, J. A.; Suard, E.; Fauth, F.; Playford, H. Y.; Dambournet, D.; Borkiewicz, O. J.; Courty, M.; Clemens, O.; Chotard, J.-N.; Islam, M. S.; Masquelier, C. Insights into the Rich Polymorphism of the Na⁺ Ion Conductor Na₃PS₄ from the Perspective of Variable-Temperature Diffraction and Spectroscopy. *Chem. Mater.* **2021**, *33*, 5652–5667.
- (15) Hogrefe, K.; Minafra, N.; Hanghofer, I.; Banik, A.; Zeier, W. G.; Wilkening, H. M. R. Opening Diffusion Pathways through Site Disorder: The Interplay of Local Structure and Ion Dynamics in the Solid Electrolyte Li_{6+x}P_{1-x}Ge_xS₅I as Probed by Neutron Diffraction and NMR. *J. Am. Chem. Soc.* **2022**, *144*, 1795–1812.
- (16) Jansen, M. Volume Effect or Paddle-Wheel Mechanism – Fast Alkali-Metal Ionic Conduction in Solids with Rotationally Disordered Complex Anions. *Angew. Chem. Int. Ed.* **1991**, *30*, 1547–1558.
- (17) Zhang, Z.; Nazar, L. F. Exploiting the Paddle-Wheel Mechanism for the Design of Fast Ion Conductors. *Nat. Rev. Mater.* **2022**, *7*, 389–405.
- (18) Smith, J. G.; Siegel, D. J. Low-Temperature Paddlewheel Effect in Glassy Solid Electrolytes. *Nat. Commun.* **2020**, *11*, 1483.
- (19) Kaup, K.; Assoud, A.; Liu, J.; Nazar, L. F. Fast Li-Ion Conductivity in Superadamantanoid Lithium Thioborate Halides. *Angew. Chem. Int. Ed.* **2021**, *60*, 6975–6980.
- (20) Buehrer, W.; Altorfer, F.; Mesot, J.; Bill, H.; Carron, P.; Smith, H. G. Lattice Dynamics and the Diffuse Phase Transition of Lithium Sulphide Investigated by Coherent Neutron Scattering. *J. Phys. Condens. Matter* **1991**, *3* 1055–1064.

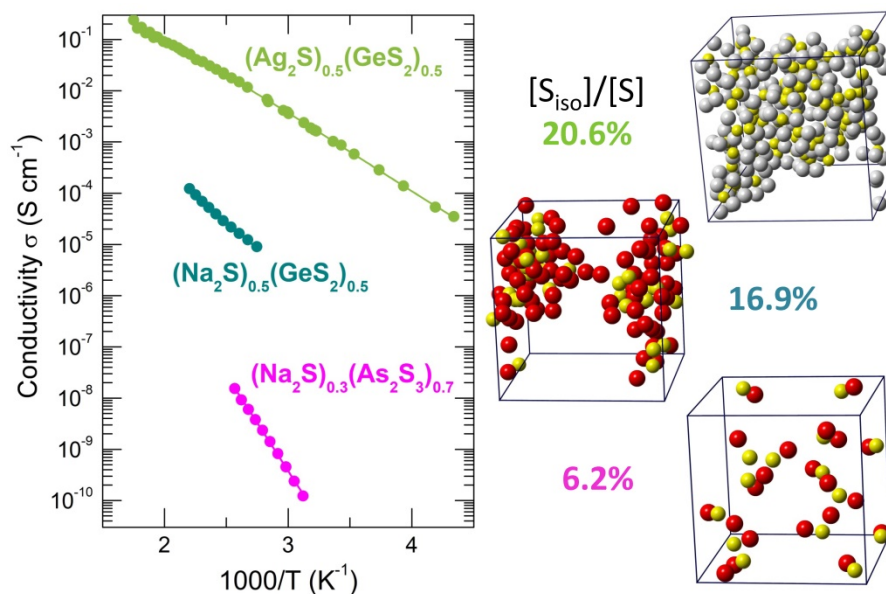
- 1
2
3 (21) Hull, S. Superionics: Crystal Structures and Conduction Processes. *Rep. Prog. Phys.* **2004**, *67*,
4 1233–1314.
- 5 (22) Möbius, H.-H.; Witzmann, H.; Härtung, R. Über die Ionenbeweglichkeit in Wasserfreiem
6 Natriumsulfid. *Z. Phys. Chem. Leipzig* **1964**, *224*, 40-55.
- 7 (23) Bertheville, B.; Lovy, D.; Bill, H.; Kubel, F. Ionic Conductivity of Na₂S Single Crystals between 295
8 and 1350 K: Experimental Setup and First Results. *J. Phys. Chem. Solids* **1997**, *58*, 1569-1577.
- 9 (24) Allen, R. L.; Moore, W. J. Diffusion of Silver in Silver Sulfide. *J. Phys. Chem.* **1959**, *63*, 223–226.
- 10 (25) Barrau, B.; Ribes, M.; Maurin, M.; Kone, A.; Souquet, J.-L. Glass Formation, Structure and Ionic
11 Conduction in the Na₂S-GeS₂ System. *J. Non-Cryst. Solids* **1980**, *37*, 1-14.
- 12 (26) Drugov, Yu.; Tsegelnik, V.; Bolotov, A.; Vlasov, Yu.; Bychkov, E. ¹¹⁰Ag Tracer Diffusion Study of
13 Percolation Transition in Ag₂S-As₂S₃ glasses. *Solid State Ionics* **2000**, *136–137*, 1091–1096.
- 14 (27) Bychkov, E. Tracer Diffusion Studies of Ion-Conducting Chalcogenide Glasses. *Solid State Ionics*
15 **2000**, *136–137*, 1111–1118.
- 16 (28) Bounazef-Legenne, T. *Verres de Chalcogénures Dopés au Sodium: Variété Chimique et Topologique*
17 *et Relation avec les Propriétés de Transport*; Ph.D. Thesis: Université du Littoral Côte d'Opale,
18 France, 2020.
- 19 (29) Alekseev, I.; Fontanari, D.; Sokolov, A.; Bokova, M.; Kassem, M.; Bychkov, E. Ionic Conductivity and
20 Tracer Diffusion in Glassy Chalcogenides. In *World Scientific Reference of Amorphous Materials*;
21 Taylor, P. C., Ed.; World Scientific: Singapore, 2020; Vol. 1, pp 203–249.
- 22 (30) Kassem, M.; Bounazef, T.; Fontanari, D.; Sokolov, A.; Bokova, M.; Hannon, A. C.; Bychkov, E.
23 Chemical and Structural Variety in Sodium Thioarsenate Glasses Studied by Neutron Diffraction
24 and Supported by First-Principles Simulations. *Inorg. Chem.* **2020**, *59*, 16410–16420.
- 25 (31) Tatsumisago, M.; Shinkuma, Y.; Minami, T. Stabilization of Superionic α-AgI at Room Temperature
26 in a Glass Matrix. *Nature* **1991**, *354*, 217–218.
- 27 (32) Funke, K.; Banhatti, R. D.; Grabowski, P.; Nowinski, J.; Wrobel, W.; Dinnebier, R.; Magdysyuk, O.
28 Low-Temperature α-AgI Confined in Glass: Structure and Dynamics. *Solid State Ionics* **2015**, *271*,
29 2–9.
- 30 (33) Gorochov, O. Les Composés Ag₈MX₆ (M= Si, Ge, Sn et X= S, Se, Te). *Bull. Soc. Chim. Fr.* **1968**, 2263–
31 2275.
- 32 (34) Susman, S.; Boehm, L.; Volin, K. J.; Delbecq, C. J. A New Method for the Preparation of Fast-
33 Conducting, Reactive Glass Systems. *Solid State Ionics* **1981**, *5*, 667–670.
- 34 (35) Foix, D.; Martinez, H.; Pradel, A.; Ribes, M.; Gonbeau, D. XPS Valence Band Spectra and Theoretical
35 Calculations for Investigations on Thiogermanate and Thiosilicate Glasses. *Chem. Phys.* **2006**, *323*,
36 606–616.
- 36 (36) Blaineau, S.; Jund, P. Structural Properties of Various Sodium Thiogermanate Glasses through
37 DFT-based Molecular Dynamics Simulations. *Phys. Rev. B* **2006**, *74*, 054203.
- 38 (37) Itoh, K.; Toshiharu Fukunaga, T. Structure of Na₂S-GeS₂ Glasses Studied by using Neutron and X-
39 ray Diffraction and Reverse Monte Carlo Modeling. *Solid State Ionics* **2009**, *180*, 351–355.
- 40 (38) Zaiter, R.; Kassem, M.; Bokova, M.; Cuisset, A.; Bychkov, E. Mercury Thiogermanate Glasses HgS-
41 GeS₂: Vibrational, Macroscopic, and Electric Properties. *J. Phys. Chem. B* **2020**, *124*, 7075–7085.
- 42 (39) Philippot, E.; Ribes, M.; Lindqvist, O. Structure Cristalline de Na₄Ge₄S₁₀. *Rev. Chim. Miner.* **1971**, *8*,
43 477-489.
- 44 (40) Olivier-Fourcade, J.; Philippot, E.; Ribes, M.; Maurin, M. Structure Cristalline du Thiogermanate de
45 Sodium Na₂GeS₃. *C. R. Hebd. Séances Acad. Sci., Serie C*, **1972**, *274*, 1185-1187.
- 46 (41) Jumas, J. C.; Olivier Fourcade, J.; Vermot-Gaud-Daniel, F.; Ribes, M.; Philippot, E.; Maurin, M. Etude
47 Structurale de Thiocomposés à Groupements Anioniques de Type -Pyro-, Na₆X₂S₇ (X = Ge, Sn) et
48 Ba₃Sn₂S₇. *Rev. Chim. Miner.* **1974**, *11*, 13-26.
- 49 (42) Kassem, M.; Bokova, M.; Tverjanovich, A.; Fontanari, D.; Le Coq, D.; Sokolov, A.; Masselin, P.;
50 Kohara, S.; Usuki, T.; Hannon, A. C.; Benmore, C. J.; Bychkov, E. Bent HgI₂ Molecules in the Melt and
51 Sulfide Glasses: Implications for Nonlinear Optics. *Chem. Mater.* **2019**, *31*, 4103–4112.
- 52 (43) Bokova, M.; Tverjanovich, A.; Benmore, C. J.; Fontanari, D.; Sokolov, A.; Khomenko, M.; Kassem, M.;
53 Ozheredov, I.; Bychkov, E. Unraveling the Atomic Structure of Bulk Binary Ga-Te Glasses with
54
55
56
57
58
59
60

- Surprising Nanotectonic Features for Phase-Change Memory Applications. *ACS Appl. Mater. Interfaces* **2021**, *13*, 37363–37379.
- (44) Hannon, A. C. Results on Disordered Materials from the General Materials Diffractometer, GEM, at ISIS. *Nucl. Instrum. Methods Phys. Res., Sect. A* **2005**, *551*, 88–107.
- (45) Hannon, A. C.; Howells, W. S.; Soper, A. K. ATLAS: A Suite of Programs for the Analysis of Time-of-Flight Neutron Diffraction Data from Liquid and Amorphous Samples. *Inst. Phys. Conf. Ser.* **1990**, *107*, 193–211.
- (46) Soper, A. K. *GudrunN and GudrunX: Programs for Correcting Raw Neutron and X-Ray Total Scattering Data to Differential Cross Section. GUDRUN Manual*; ISIS Spallation Source, 2017 (<https://www.isis.stfc.ac.uk/OtherFiles/Disordered%20Materials/Gudrun-Manual-2017-10.pdf>).
- (47) Alekseev, I.; Kassem, M.; Fourmentin, M.; Le Coq, D.; Iizawa, R.; Usuki, T.; Bychkov, E. Ionic and electronic transport in AgI–As₂Te₃ glasses. *Solid State Ionics* **2013**, *253*, 181–184.
- (48) Kassem, M.; Alekseev, I.; Bokova, M.; Le Coq, D.; Bychkov, E. Ionic-to-Electronic Conductivity Crossover in CdTe–AgI–As₂Te₃ Glasses: An ^{110m}Ag Tracer Diffusion Study. *J. Phys. Chem. B* **2018**, *122*, 4179–4186.
- (49) Frisch, M. J.; Trucks, G. W.; Schlegel, H. B.; Scuseria, G. E.; Robb, M. A.; Cheeseman, J. R.; Scalmani, G.; Barone, V.; Petersson, G. A.; Nakatsuji, H.; Li, X.; Caricato, M.; Marenich, A. V.; Bloino, J.; Janesko, B. G.; Gomperts, R.; Mennucci, B.; Hratchian, H. P.; Ortiz, J. V.; Izmaylov, A. F.; Sonnenberg, J. L.; Williams-Young, D.; Ding, F.; Lipparini, F.; Egidi, F.; Goings, J.; Peng, B.; Petrone, A.; Henderson, T.; Ranasinghe, D.; Zakrzewski, V. G.; Gao, J.; Rega, N.; Zheng, G.; Liang, W.; Hada, M.; Ehara, M.; Toyota, K.; Fukuda, R.; Hasegawa, J.; Ishida, M.; Nakajima, T.; Honda, Y.; Kitao, O.; Nakai, H.; Vreven, T.; Throssell, K.; Montgomery, J. A.; Peralta, J. E.; Ogliaro, F.; Bearpark, M. J.; Heyd, J. J.; Brothers, E. N.; Kudin, K. N.; Staroverov, V. N.; Keith, T. A.; Kobayashi, R.; Normand, J.; Raghavachari, K.; Rendell, A. P.; Burant, J. C.; Iyengar, S. S.; Tomasi, J.; Cossi, M.; Millam, J. M.; Klene, M.; Adamo, C.; Cammi, R.; Ochterski, J. W.; Martin, R. L.; Morokuma, K.; Farkas, O.; Foresman, J. B.; Fox, D. J. *Gaussian 16*, revision B.01; Gaussian, Inc.: Wallingford, CT, 2016.
- (50) Becke, A. D. Density-Functional Thermochemistry. III. The Role of Exact Exchange. *J. Chem. Phys.* **1993**, *98*, 5648–5653.
- (51) Lee, C.; Yang, W.; Parr, R. G. Development of the Colle-Salvetti Correlation-Energy Formula into a Functional of the Electron Density. *Phys. Rev. B* **1988**, *37*, No. 785.
- (52) Feller, D. The Role of Databases in Support of Computational Chemistry Calculations. *J. Comput. Chem.* **1996**, *17*, 1571–1586.
- (53) Peterson, K. A.; Figgen, D.; Goll, E.; Stoll, H.; Dolg, M. Systematically Convergent Basis Sets with Relativistic Pseudopotentials. II. Small-Core Pseudopotentials and Correlation Consistent Basis Sets for the Post-d Group 16–18 Elements. *J. Chem. Phys.* **2003**, *119*, 11113–11123.
- (54) Bacskay, G. B. A Quadratically Convergent Hartree-Fock (QCSCF) Method. Application to Closed Shell Systems. *Chem. Phys.* **1981**, *61*, 385–404.
- (55) Masselin, P.; Le Coq, D.; Cuisset, A.; Bychkov, E. Spatially Resolved Raman Analysis of Laser Induced Refractive Index Variation in Chalcogenide Glass. *Opt. Mater. Express* **2012**, *2*, 1768–1775.
- (56) Tverjanovich, A.; Cuisset, A.; Fontanari, D.; Bychkov, E. Structure of Se-Te Glasses by Raman Spectroscopy and DFT Modelling. *J. Am. Ceram. Soc.* **2018**, *101*, 5188–5197.
- (57) Kühne, T. D.; Iannuzzi, M.; Del Ben, M.; Rybkin, V. V.; Seewald, P.; Stein, F.; Laino, T.; Khaliullin, R. Z.; Schütt, O.; Schiffmann, F.; Golze, D.; Wilhelm, J.; Chulkov, S.; Bani-Hashemian, M. H.; Weber, V.; Borštnik, U.; Taillefumier, M.; Jakobovits, A. S.; Lazzaro, A.; Pabst, H.; Müller, T.; Schade, R.; Guidon, M.; Andermatt, S.; Holmberg, N.; Schenter, G. K.; Hehn, A.; Bussy, A.; Belleflamme, F.; Tabacchi, G.; Glöß, A.; Lass, M.; Bethune, I.; Mundy, C. J.; Plessl, C.; Watkins, M.; VandeVondele, J.; Krack, M.; Hutter, J. CP2K: An Electronic Structure and Molecular Dynamics Software Package – Quickstep: Efficient and Accurate Electronic Structure Calculations. *J. Chem. Phys.* **2020**, *152*, 194103.
- (58) Perdew, J. P.; Ernzerhof, M.; Burke, K. Rationale for Mixing Exact Exchange with Density Functional Approximations. *J. Chem. Phys.* **1996**, *105*, 9982–9985.

- 1
2
3 (59) Adamo, C.; Barone, V. Toward Reliable Density Functional Methods without Adjustable
4 Parameters: The PBE0 Model. *J. Chem. Phys.* **1999**, *110*, 6158–6170.
- 5 (60) Grimme, S.; Ehrlich, S.; Goerigk, L. Effect of the Damping Function in Dispersion Corrected Density
6 Functional Theory. *J. Comput. Chem.* **2011**, *32*, 1456–1465.
- 7 (61) Micoulaut, M. Communication: Van der Waals Corrections for an Improved Structural Description
8 of Telluride Based Materials. *J. Chem. Phys.* **2013**, *138*, 061103.
- 9 (62) Bouzid, A.; Massobrio, C.; Boero, M.; Ori, G.; Sykina, K.; Furet, E. Role of the van der Waals
10 Interactions and Impact of the Exchange-Correlation Functional in Determining the Structure of
11 Glassy GeTe₄. *Phys. Rev. B* **2015**, *92*, 134208.
- 12 (63) Akola, J.; Jones, R. O.; Kohara, S.; Kimura, S.; Kobayashi, K.; Takata, M.; Matsunaga, T.; Kojima, R.;
13 Yamada, N. Experimentally Constrained Density-Functional Calculations of the Amorphous
14 Structure of the Prototypical Phase-Change Material Ge₂Sb₂Te₅. *Phys. Rev. B* **2009**, *80*, 020201.
- 15 (64) Matsunaga, T.; Akola, J.; Kohara, S.; Honma, T.; Kobayashi, K.; Ikenaga, E.; Jones, R. O.; Yamada, N.;
16 Takata, M.; Kojima, R. From Local Structure to Nanosecond Recrystallization Dynamics in
17 AgInSbTe Phase-Change Materials. *Nat. Mater.* **2011**, *10*, 129–134.
- 18 (65) Gereben, O.; Pusztai, L. RMC_POT, a Computer Code for Reverse Monte Carlo Modeling the
19 Structure of Disordered Systems Containing Molecules of Arbitrary Complexity. *J. Comput. Chem.*
20 **2012**, *33*, 2285–2291.
- 21 (66) Hartwigsen, C.; Goedecker, S.; Hutter, J. Relativistic Separable Dual-Space Gaussian Pseudo-
22 potentials from H to Rn. *Phys. Rev. B* **1998**, *58*, 3641.
- 23 (67) Le Roux, S.; Jund, P. Ring Statistics Analysis of Topological Networks: New Approach and
24 Application to Amorphous GeS₂ and SiO₂ Systems. *Comput. Mater. Sci.* **2010**, *49*, 70–83.
- 25 (68) Kohara, S.; Ohno, H.; Takata, M.; Usuki, T.; Morita, H.; Suzuya, K.; Akola, J.; Pusztai, L. Lead Silicate
26 Glasses: Binary Network-Former Glasses with Large Amounts of Free Volume. *Phys. Rev. B* **2010**,
27 *82*, 134209.
- 28 (69) Heimbach, I.; Rhiem, F.; Beule, F.; Knodt, D.; Heinen, J.; Jones, R. O. pyMolDyn: Identification,
29 Structure, and Properties of Cavities/Vacancies in Condensed Matter and Molecules. *J. Comput.*
30 *Chem.* **2017**, *38*, 389–394.
- 31 (70) Dittmar, G.; Schaefer, H. Die Kristallstruktur von H.T.-GeS₂. *Acta Crystallogr., Sect. B* **1975**, *31*,
32 2060-2064.
- 33 (71) Bonneau, P. R.; Jarvis, R. F. jr.; Kaner, R. B. Solid-State Metathesis as a Quick Route to Transition-
34 Metal Mixed Dichalcogenides. *Inorg. Chem.* **1992**, *31*, 2127-2132.
- 35 (72) Jackson, K.; Briley, A.; Grossman, S.; Porezag, D. V.; Pederson, M. R. Raman-Active Modes of α-GeSe₂
36 and α-GeS₂: A First-Principles Study. *Phys. Rev. B* **1999**, *60*, R14985-14989.
- 37 (73) Blaineau, S.; Jund, P. Vibrational Signature of Broken Chemical Order in a GeS₂ Glass: A Molecular
38 Dynamics Simulation. *Phys. Rev. B* **2004**, *69*, 064201.
- 39 (74) Holomb, R.; Johansson, P.; Mitsa, V.; Rosola, I. Local Structure of Technologically Modified g-GeS₂:
40 Resonant Raman and Absorption Edge Spectroscopy Combined with Ab Initio Calculations. *Phil.*
41 *Mag.* **2005**, *85*, 2947-2960.
- 42 (75) Boolchand, P.; Grothaus, J.; Tenhover, M.; Hazle, M. A.; Grasselli, R. K. Structure of GeS₂ Glass:
43 Spectroscopic Evidence for Broken Chemical Order. *Phys. Rev. B* **1986**, *33*, 5421-5434.
- 44 (76) Bychkov E.; Miloshova M.; Price D. L.; Benmore C. J.; Lorriaux A. Short, Intermediate and
45 Mesoscopic Range Order in Sulphur-Rich Binary Glasses. *J. Non-Cryst. Solids* **2006**, *352*, 63-70.
- 46 (77) Montaner, A.; Galtier, M.; Benoit, C.; Bill, H. Optical Constants of Sodium Sulphide. *Phys. Stat. Solidi*
47 *A* **1979**, *52*, 597–601.
- 48 (78) Janz, G. J.; Downey, J. R. jr.; Roduner, E.; Wasilczyk, G. J.; Coutts, J. W.; Elauard, A. Raman Studies of
49 Sulfur-Containing Anions in Inorganic Polysulfides. Sodium Polysulfides. *Inorg. Chem.* **1976**, *15*,
50 1759–1763.
- 51 (79) Böttcher, P.; Getzschmann, J.; Keller, R. Zur Kenntnis der Dialkalimetalldichalkogenide β-Na₂S₂,
52 K₂S₂, α-Rb₂S₂, β-Rb₂S₂, K₂Se₂, Rb₂Se₂, α-K₂Te₂, β-K₂Te₂ und Rb₂Te₂. *Z. Anorg. Allg.*
53 *Chem.* **1993**, *619*, 476–478.
- 54
55
56
57
58
59
60

- 1
2
3 (80) Berbano S. S.; Seo, I.; Bischoff, C. M.; Schuller, K. E.; Martin, S. W. Formation and Structure of
4 $\text{Na}_2\text{S}+\text{P}_2\text{S}_5$ Amorphous Materials Prepared by Melt-Quenching and Mechanical Milling. *J. Non-*
5 *Cryst. Solids* **2012**, *358*, 93–98.
- 6 (81) Bühner, W.; Bill, H. Lattice Dynamics of Na_2S . *J. Phys. C: Solid State Phys.* **1980**, *13*, 5495–5504.
- 7 (82) Bychkov, A.; Cuello, G. J.; Kohara, S.; Benmore, C. J.; Price, D. L.; Bychkov, E. Unraveling the Atomic
8 Structure of Ge-Rich Sulfide Glasses. *Phys. Chem. Chem. Phys.* **2013**, *15*, 8487–8494.
- 9 (83) Bychkov, E.; Benmore, C. J.; Price, D. L. Compositional Changes of the First Sharp Diffraction Peak
10 in Binary Selenide Glasses. *Phys. Rev. B* **2005**, *72*, No. 172107.
- 11 (84) Zeidler, A.; Drewitt, J. W. E.; Salmon, P. S.; Barnes, A. C.; Crichton, W. A.; Klotz, S.; Fischer, H. E.;
12 Benmore, C. J.; Ramos, S.; Hannon, A. C. Establishing the Structure of GeS_2 at High Pressures and
13 Temperatures: A Combined Approach using X-ray and Neutron Diffraction. *J. Phys.: Condens.*
14 *Matter* **2009**, *21*, No. 474217.
- 15 (85) Wiedemeier H.; von Schnering, H. G. Refinement of the Structures of GeS, GeSe, SnS and SnSe. *Z.*
16 *Kristallogr.* **1978**, *148*, 295–303.
- 17 (86) Chau, P.-L.; Hardwick, A. J. A New Order Parameter for Tetrahedral Configurations. *Mol. Phys.*
18 **1998**, *93*, 511–518.
- 19 (87) Errington, J. R.; Debenedetti, P. G. Relationship between Structural Order and the Anomalies of
20 Liquid Water. *Nature* **2001**, *409*, 318–321.
- 21 (88) Caravati, S.; Bernasconi, M.; Kühne, T. D.; Krack, M.; Parrinello, M. Coexistence of Tetrahedral- and
22 Octahedral-Like Sites in Amorphous Phase Change Materials. *Appl. Phys. Lett.* **2007**, *91*, No.
23 171906.
- 24 (89) Tverjanovich, A.; Khomenko, M.; Benmore, C. J.; Bokova, M.; Sokolov, A.; Fontanari, D.; Kassem, M.;
25 Usuki, T.; Bychkov, E. Bulk Glassy GeTe_2 : A Missing Member of the Tetrahedral GeX_2 Family and a
26 Precursor for the Next Generation of Phase-Change Materials. *Chem. Mater.* **2021**, *33*, 1031–1045.
- 27 (90) Tverjanovich, A.; Khomenko, M.; Benmore, C. J.; Bereznev, S.; Sokolov, A.; Fontanari, F.; Kiselev, A.;
28 Lotin, A.; Bychkov, E. Atypical Phase-Change Alloy Ga_2Te_3 : Atomic Structure, Incipient
29 Nanotectonic Nuclei, and Multilevel Writing. *J. Mater. Chem. C* **2021**, *9*, 17019–17032.
- 30 (91) Huang, R.; Chavez, I.; Taute, K. M.; Lukić, B.; Jeney, S.; Raizen, M. G.; Florin, E.-L. Direct Observation
31 of the Full Transition from Ballistic to Diffusive Brownian Motion in a Liquid. *Nat. Phys.* **2011**, *7*,
32 576–580.
- 33 (92) Berthier L.; Biroli, G. Theoretical Perspective on the Glass Transition and Amorphous Materials.
34 *Rev. Modern Phys.* **2011**, *83*, 587–645.
- 35 (93) Tverjanovich, A.; Khomenko, M.; Bereznev, S.; Fontanari, D.; Sokolov, A.; Usuki, T.; Ohara, K.; Le
36 Coq, D.; Masselin, P.; Bychkov, E. Glassy GaS: Transparent and Unusually Rigid Thin Films for
37 Visible to Mid-IR Memory Applications. *Phys. Chem. Chem. Phys.* **2020**, *22*, 25560–25573.
- 38 (94) Hori, S.; Kanno, R.; Kwon, O.; Kato, Y.; Yamada, T.; Matsuura, M.; Yonemura, M.; Kamiyama, T.;
39 Shibata, K.; Kawakita, Y. Revealing the Ion Dynamics in $\text{Li}_{10}\text{GeP}_2\text{S}_{12}$ by Quasi-Elastic Neutron
40 Scattering Measurements. *J. Phys. Chem. C* **2022**, <https://doi.org/10.1021/acs.jpcc.2c01748>
- 41 (95) Habasaki, J.; Leon, C.; Ngai, K. L. *Dynamics of Glassy, Crystalline and Liquid Ionic Conductors*;
42 Springer: Heidelberg, 2017; pp 435–444.
- 43 (96) Hannon, A. C. XTAL: a Program for Calculating Interatomic Distances and Coordination Numbers
44 for Model Structures. Rutherford-Appleton Laboratory Report RAL-93-063; 1993
45 (<http://www.wisis2.isis.rl.ac.uk/disordered/ACH/Software/xtal.htm>).
- 46 (97) Soignard, E.; Tsiok, O. B.; Tverjanovich, A. S.; Bychkov, A.; Sokolov, A.; Brazhkin, V. V.; Benmore, C.
47 J.; Bychkov, E. Pressure-Driven Chemical Disorder in Glassy As_2S_3 up to 14.7 GPa,
48 Postdensification Effects, and Applications in Materials Design. *J. Phys. Chem. B* **2020**, *124*,
49 430–442.
- 50 (98) Tsunetomo, K.; Sugishima, T.; Imura, T.; Osaka, Y. Stability of Metastable GeTe_2 in Thin Films. *J.*
51 *Non-Cryst. Solids* **1987**, *95–96*, 509–516.
- 52 (99) Fukumoto, H.; Tsunetomo, K.; Imura, T.; Osaka, Y. Structural Changes of Amorphous GeTe_2 Films
53 by Annealing (Formation of Metastable Crystalline GeTe_2 Films). *J. Phys. Soc. Jpn.* **1987**, *56*,
54 158–162.
- 55
56
57
58
59
60

TOC Figure and synopsis



Stoichiometry limits of crystalline systems are violated in vitreous sodium and silver sulfides leading to emerging isolated sulfur S_{iso} , that is, the sulfur species surrounded exclusively by mobile cations with a typical stoichiometry $M/S_{\text{iso}} \approx 2$. The $S_{\text{iso}}/S_{\text{tot}}$ fraction appears to be a reliable descriptor of fast ion transport in glassy systems over a wide range of ionic conductivities and cation diffusivities.

Supporting Information

Deciphering Fast Ion Transport in Glasses: a Case Study of Sodium and Silver Vitreous Sulfides

Mohammad Kassem,¹ Tinehinane Bounazef,¹ Anton Sokolov,¹ Maria Bokova,¹ Daniele Fontanari,¹ Alex C. Hannon,² Igor Alekseev,¹ and Eugene Bychkov*,¹

¹ *Université du Littoral Côte d'Opale, 59140 Dunkerque, France*

² *ISIS Facility, Rutherford Appleton Laboratory, Chilton, Didcot, OX11 0QX, U.K.*

Figure S1. Ionic conductivity of vitreous sodium and silver thioarsenates, sodium thiogermanate and thiogallate.

Figure S2. Typical gamma-spectrum of ²²Na tracer.

Figure S3. Typical ²²Na tracer diffusion profile.

Figure S4. Ge-S(t) stretching as a function of x in the $(\text{Na}_2\text{S})_x(\text{GeS}_2)_{1-x}$ glasses.

Figure S5. Integration procedure for Raman spectra of $(\text{Na}_2\text{S})_x(\text{GeS}_2)_{1-x}$ glasses.

Figure S6. Ge-Ge and S-S stretching in Raman spectra of $(\text{Na}_2\text{S})_x(\text{GeS}_2)_{1-x}$ glasses.

Figure S7. Experimental and DFT Raman spectra of Na-S and S-S stretching in glasses.

Figure S8. DFT Raman spectra of size-limited Ge-S and Na-Ge-S clusters.

Figure S9. Orientational order parameter q for trigonal and tetrahedral Ge species.

Figure S10. Bond angle distributions for trigonal and tetrahedral Ge species.

Figure S11. Small Ge-S fragments forming a disconnected Ge-S subnetwork in glassy $(\text{Na}_2\text{S})_{0.5}(\text{GeS}_2)_{0.5}$.

Figure S12. Connectivity of $\text{Ge}_{3\text{F-S}}$ and $\text{Ge}_{4\text{F-S}}$ subsets.

Figure S13. Gallium mean-square displacements in GaS at 1000 K.

Tables S1 and S2. Optimized geometry of DFT clusters

* Email: Eugene.Bychkov@univ-littoral.fr

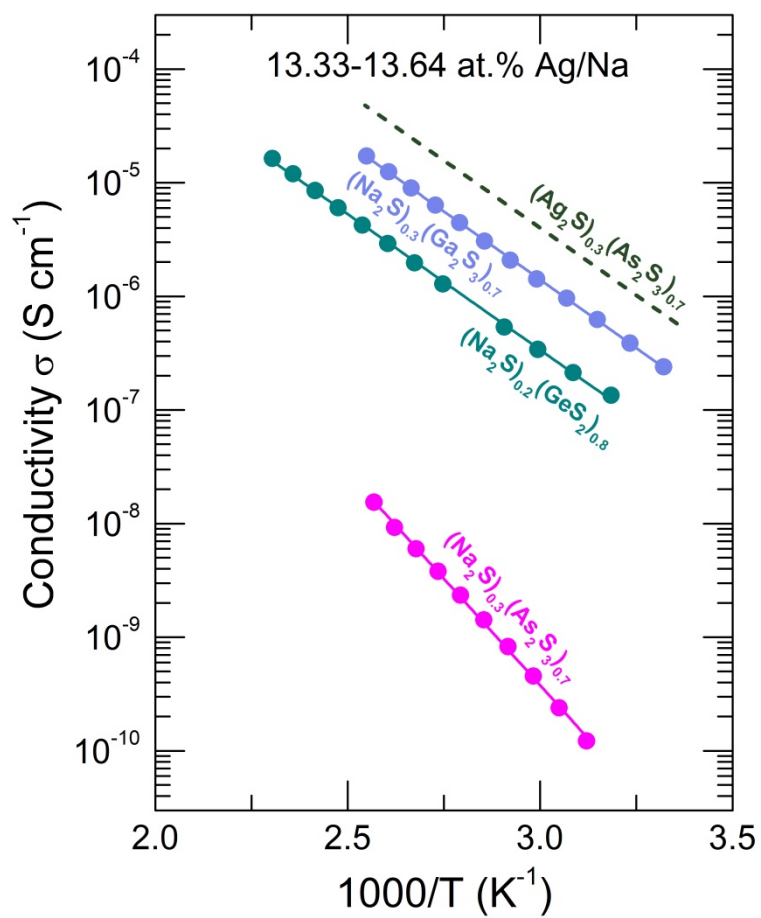


Figure S1. Ionic conductivity of vitreous $(\text{Na}_2\text{S})_{0.3}(\text{As}_2\text{S}_3)_{0.7}$ (13.64 at.% Na),^{S1} $(\text{Na}_2\text{S})_{0.2}(\text{GeS}_2)_{0.8}$ (13.33 at.% Na),^{S1} $(\text{Na}_2\text{S})_{0.3}(\text{Ga}_2\text{S}_3)_{0.7}$ (13.64 at.% Na),^{S1} and $(\text{Ag}_2\text{S})_{0.3}(\text{As}_2\text{S}_3)_{0.7}$ (13.64 at.% Ag).^{S2}

²²Na Tracer Diffusion Experimental Details

A high-purity Ge detector GX1018 and LYNX gamma-spectrometer (Canberra Ind., USA) were used to measure the initial and residual gamma activity of the sample before and after sectioning. Spectrometer calibration in the energy range from 20 keV to 1600 keV was carried out using ¹⁰⁹Cd, ¹⁵²Eu, and ²⁴¹Am sources. The gamma activity of the samples was determined using two characteristic photopeaks at 511 and 1275 keV, Figure S2.

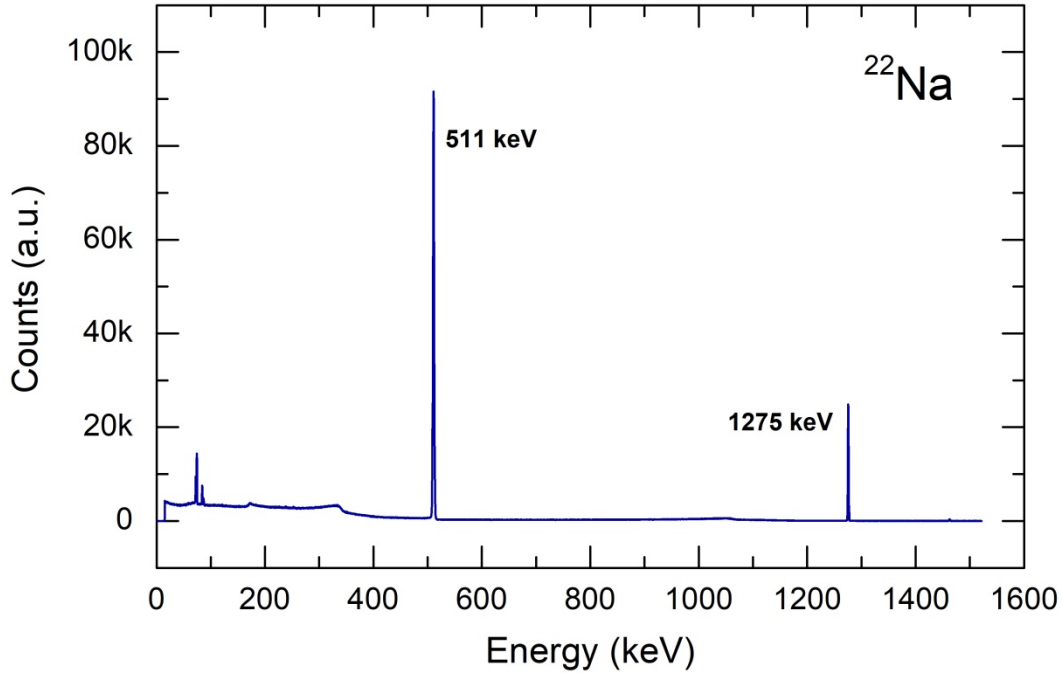


Figure S2. Typical gamma-spectrum of ²²Na tracer with two characteristic photopeaks at 511 and 1275 keV used for data collection and analysis.

The samples were placed in a polyethylene cell (the radioactive face in the bottom) in a well-defined fixed geometry. The measurements of the initial A_0 and residual $A(t)$ gamma activity were carried out for 1000 s. A Genie 2000 program (Canberra Ind., USA) was used for data analysis.

Penetration profiles for ²²Na tracer diffusion in a $(\text{Na}_2\text{S})_{0.01}(\text{As}_2\text{S}_3)_{0.99}$ glass obey the usual solution of Fick's law for an infinitesimally thin deposit of radioactive isotope on a semi-infinite specimen^{S3}

$$1 - \frac{A(X,t)}{A_0} = \text{erf}(q), \quad (\text{S1})$$

and

$$q = \frac{X}{2\sqrt{D_{\text{Na}}t}}, \quad (\text{S2})$$

where $A(X,t)$ is the residual activity of the sample after a thickness X was removed, t is the diffusion anneal time, D_{Na} the tracer diffusion coefficient, and $\text{erf}(q)$ is the Gauss error function.

Experimentally determined values of A_0 and $A(X,t)$ yield q -values which, when plotted vs. X , produce a straight line passing through origin, Figure S3.

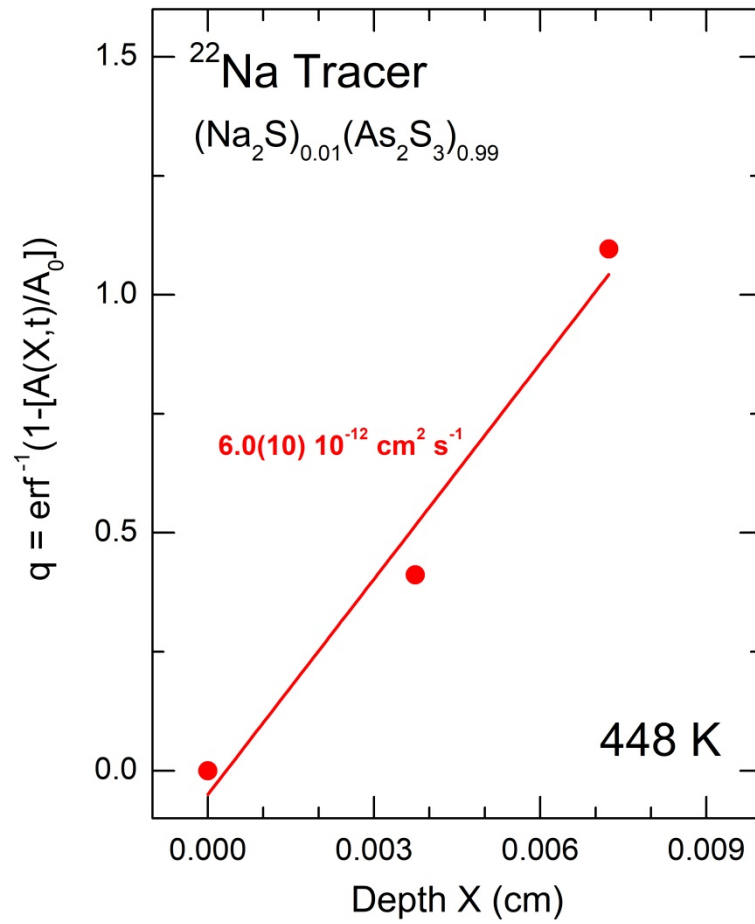


Figure S3. Typical ^{22}Na tracer diffusion profile for a $(\text{Na}_2\text{S})_{0.01}(\text{As}_2\text{S}_3)_{0.99}$ glass annealed at 448 K for 20 days. The solid line shows a least-square fit of the experimental data points to Eq. (S2), where $q = \text{erf}^{-1}(1 - \frac{A(X,t)}{A_0})$.

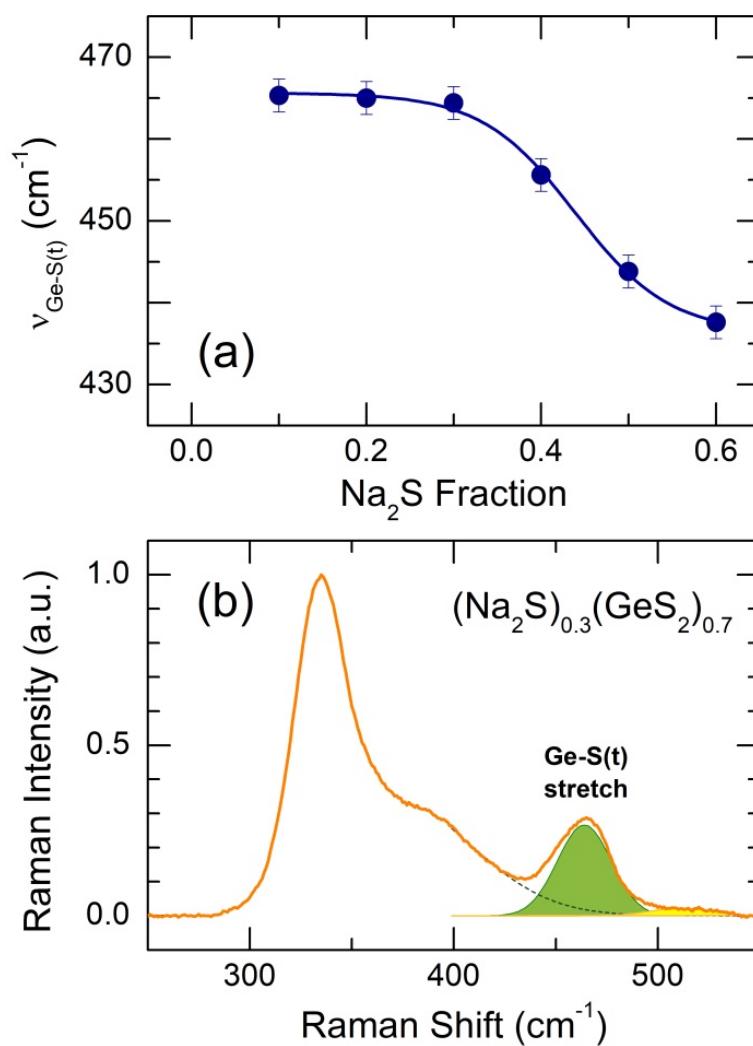


Figure S4. Ge-S(t) stretching as a function of x in the $(\text{Na}_2\text{S})_x(\text{GeS}_2)_{1-x}$ glasses: (a) composition dependence of the Ge-S(t) stretching frequency, (b) typical fitting procedure to extract the Ge-S(t) stretching position.

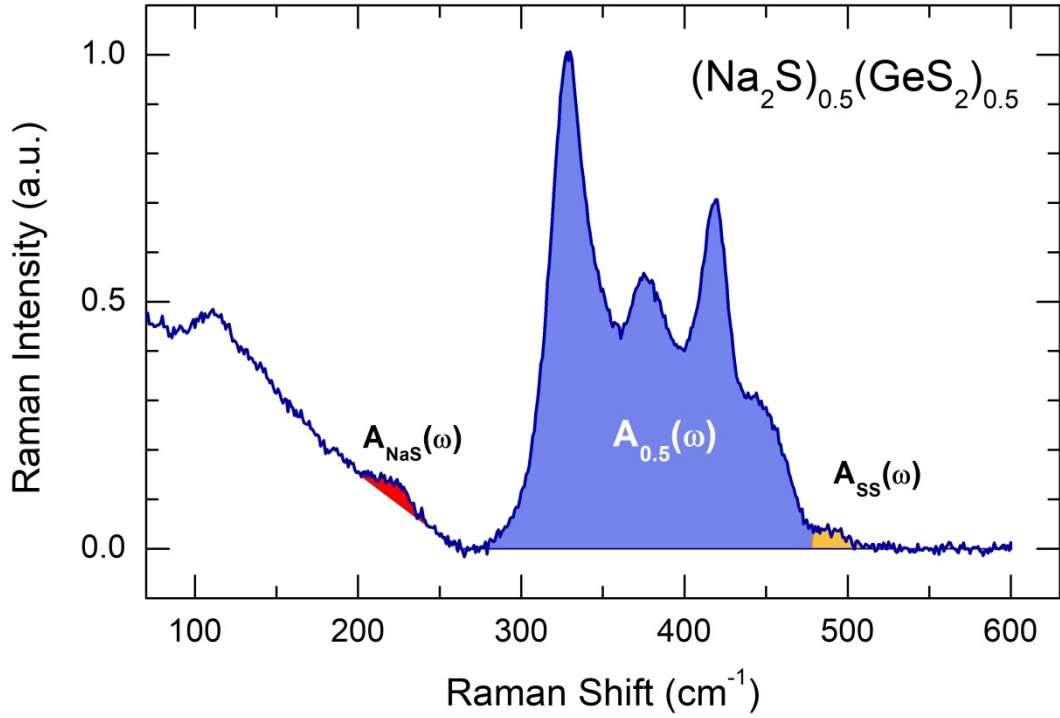


Figure S5. Integration procedure for Raman spectra of $(\text{Na}_2\text{S})_x(\text{GeS}_2)_{1-x}$ glasses, taking the equimolar glass, $x = 0.5$, as an example.

The fractional area of the S-S stretching was determined using integration

$$f_{\text{SS}}(\omega) = \frac{\int_{\omega_{\text{SS}}}^{\omega_{\text{max}}} I_x(\omega) d\omega}{\int_{\omega_{\text{min}}}^{\omega_{\text{max}}} I_x(\omega) d\omega} = \frac{A_{\text{SS}}(\omega)}{A_x(\omega)}, \quad (\text{S3})$$

where $I_x(\omega)$ represents the normalized Raman spectrum of a Na_2S - GeS_2 glass, $460 \text{ cm}^{-1} \leq \omega_{\text{SS}} \leq 490 \text{ cm}^{-1}$ depending on x , $\omega_{\text{min}} = 260 \text{ cm}^{-1}$ and $\omega_{\text{max}} = 600 \text{ cm}^{-1}$. The integrated area of the S-S stretching modes, $A_{\text{SS}}(\omega)$, is highlighted in yellow in Figure S5; the summarized integrated area of the Ge-S and S-S stretching features, $A_x(\omega)$, is depicted in blue.

The fractional area of the Na-S stretching was also determined by integration, as it is shown in Figure S5. In this case, we did not use a Gaussian least-square fitting similar to that in Figure S4 for Ge-S(t) stretching. Consequently, $f_{\text{NaS}}(\omega)$ seems to be underestimated but can be used qualitatively.

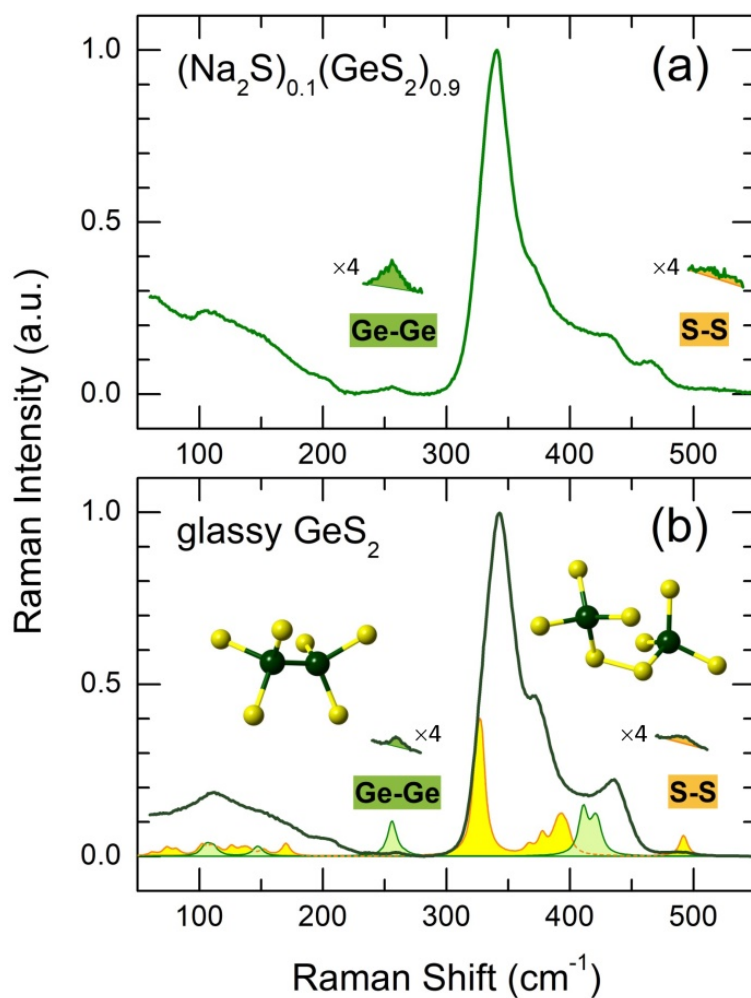


Figure S6. Ge-Ge and S-S stretching in Raman spectra of glassy (a) $(\text{Na}_2\text{S})_{0.1}(\text{GeS}_2)_{0.9}$ and (b) GeS_2 plotted together with DFT spectra of ethane-like $\text{ETH-Ge}_2\text{S}_6\text{H}_6$ and $\text{CS-Ge}_2\text{S}_8\text{H}_6$ clusters (the insets in Figure S6b). Terminal hydrogen species are not shown, and H-related vibrations are removed from the spectra.

The DFT modeling of ethane-like $\text{ETH-Ge}_2\text{S}_6\text{H}_6$ cluster confirms the Ge-Ge stretching at $\approx 250 \text{ cm}^{-1}$, while DFT-optimized $\text{CS-Ge}_2\text{S}_8\text{H}_6$ cluster, including S-S dimer, shows S-S stretching at $\approx 490 \text{ cm}^{-1}$.

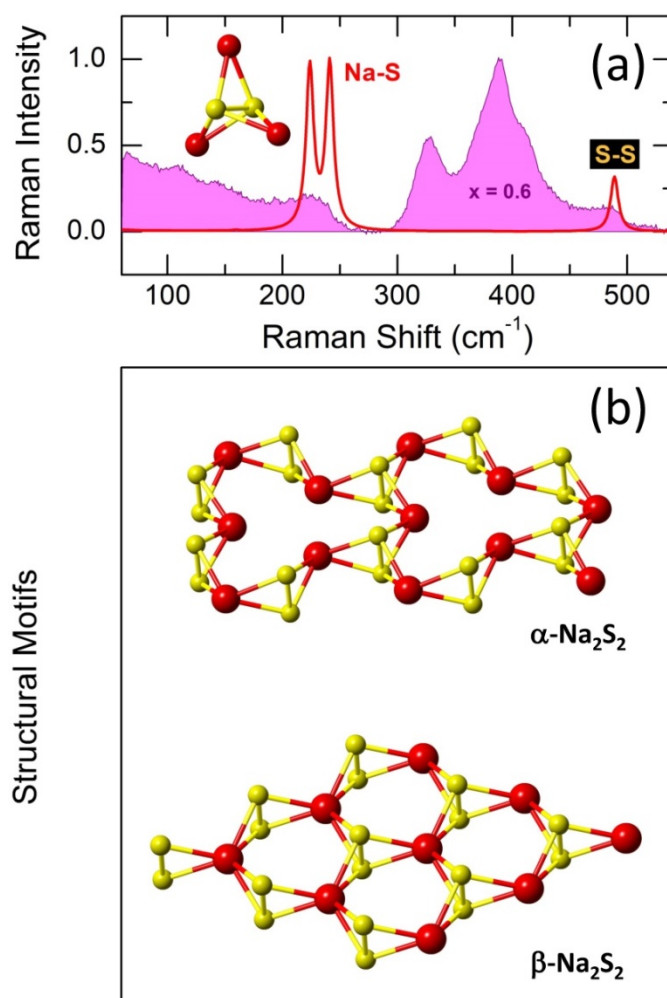


Figure S7. (a) Experimental Raman spectrum of glassy (Na₂S)_{0.6}(GeS₂)_{0.4} (highlighted in magenta) and calculated spectrum of DFT-optimized S₂Na₃ cluster (the red line) revealing Na-S and S-S stretching vibrations between $224 \leq \omega_{\text{Na-S}} \leq 242 \text{ cm}^{-1}$ and at $\omega_{\text{S-S}} \approx 489 \text{ cm}^{-1}$, respectively; (b) structural motifs in α - and β -polymorphs of Na₂S₂.^{S4} The S₂Na₃ cluster is also shown in (a).

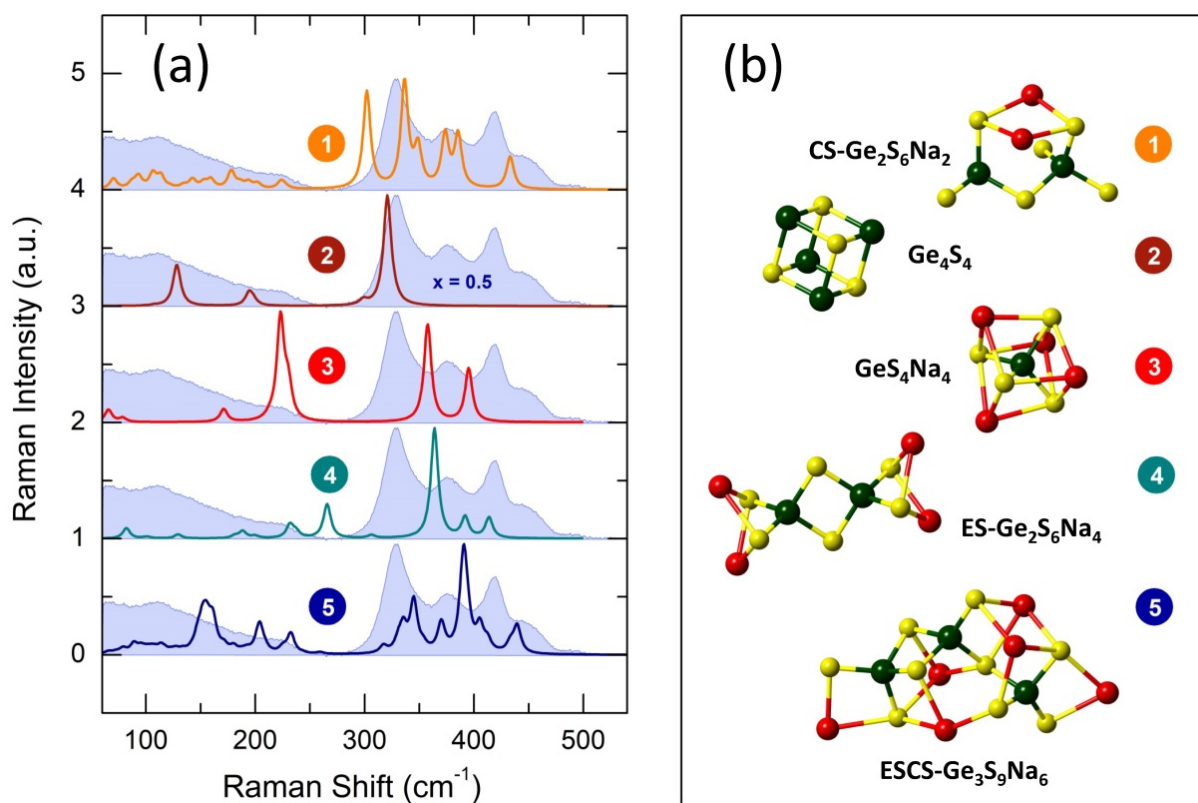


Figure S8. (a) DFT Raman spectra of size-limited Ge-S and Na-Ge-S clusters in comparison with experimental data for glassy equimolar $(\text{Na}_2\text{S})_{0.6}(\text{GeS}_2)_{0.4}$, highlighted in light blue; (b) schematic representation of optimized clusters: (1) corner-sharing CS- $\text{Ge}_2\text{S}_6\text{H}_3$ (the terminal hydrogen species are not shown, the H-related vibrations are removed from the calculated spectrum), (2) Ge_4S_4 , (3) GeS_4Na_4 , (4) edge-sharing ES- $\text{Ge}_2\text{S}_6\text{Na}_4$, (5) ES/CS- $\text{Ge}_3\text{S}_9\text{Na}_6$.

The tetrahedral shape and orientational order parameter q

The tetrahedral shape of GeX_4 entities clearly shows the orientational order parameter q ,^{S5,S6} extended beyond the tetrahedral geometry^{S7}

$$q = 1 - \frac{3}{8} \sum_{j=1}^{n-1} \sum_{k=j+1}^n \left(\cos \psi_{jk} + \frac{1}{3} \right)^2, \quad (\text{S4})$$

where ψ_{jk} is the X-Ge-X angle of a given GeX_n unit. The average q -value changes between 0 for an ideal gas and $q = 1$ for a regular tetrahedral network ($n = 4$). The distorted tetrahedral geometry is characterized by $0.8 \lesssim q < 1$.^{S7-S10} The probability distribution $P(q)$ for GeX_4 entities is peaked at $q = 0.96$ with a low- q tail mostly expanding up to $q = 0.86$, Figure S9b. The non-tetrahedral fraction, centered at $q \approx 0.60 \pm 0.05$ and corresponding to defect octahedral species, $q_{\text{O}_h} = 5/8$, is negligible, 2.6%. Basically, the GeX_4 tetrahedra are slightly more distorted than those in monoclinic Na_2GeS_3 , $q = 0.9514$, confirmed also by the S-Ge_{4F}-S bond angle distribution $B_{\text{SGeS}}(\theta)$, Figure S10b. We note however a low- θ shoulder at 92° in addition to the $B_{\text{SGeS}}(\theta)$ maximum at 109.9° , indicating the presence of ES- GeS_4 entities, similar to those in monoclinic HT- GeS_2 .^{S11} In contrast to tetrahedral germanium, the GeX_3 trigonal pyramids are highly distorted in comparison with orthorhombic GeS evidenced by $P(q)$, Figure S9a, and $B_{\text{SGeS}}(\theta)$, Figure S10a.

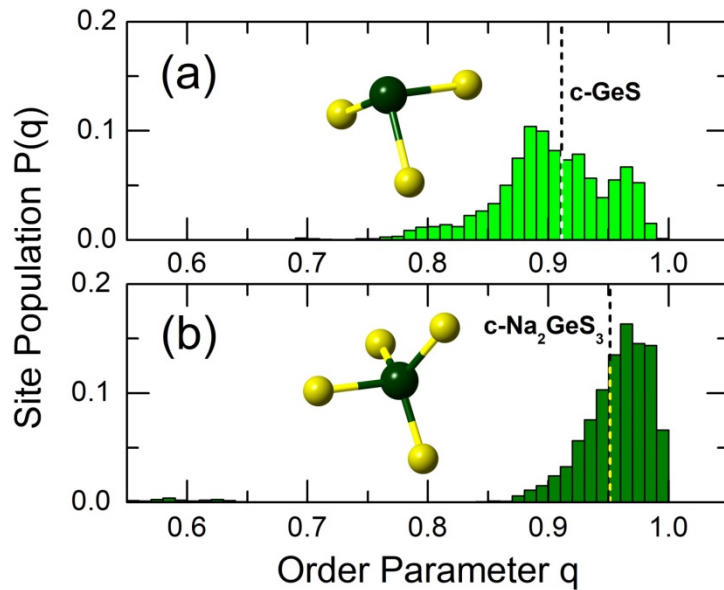


Figure S9. Orientational order parameter q for (a) three-fold $\text{Ge}_{3\text{F}}$ and (b) four-fold coordinated $\text{Ge}_{4\text{F}}$ germanium species. The q -parameters for crystalline GeS and Na_2GeS_3 are also shown.

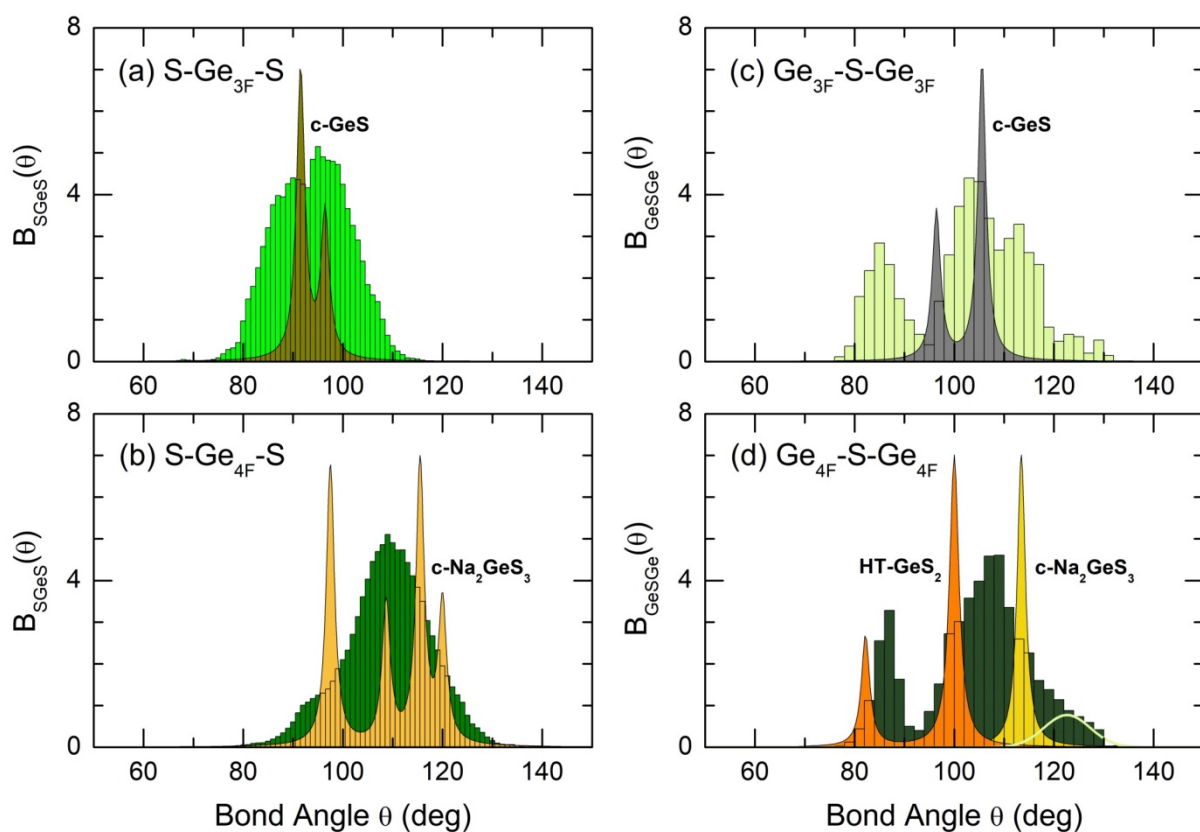


Figure S10. Bond angle distributions $B_{S\text{Ge}_3\text{F}}(\theta)$ and $B_{\text{Ge}_3\text{F-S-Ge}_3\text{F}}(\theta)$ for trigonal $\text{Ge}_{3\text{F}}$ and tetrahedral $\text{Ge}_{4\text{F}}$ species: (a) $\text{S-Ge}_{3\text{F}}\text{-S}$, (b) $\text{S-Ge}_{4\text{F}}\text{-S}$, (c) $\text{Ge}_{3\text{F}}\text{-S-Ge}_{3\text{F}}$, and (d) $\text{Ge}_{4\text{F}}\text{-S-Ge}_{4\text{F}}$. The angular distributions for crystalline references are also shown: orthorhombic GeS ,^{S12} monoclinic Na_2GeS_3 ,^{S13} and high-temperature HT-GeS_2 .^{S11}

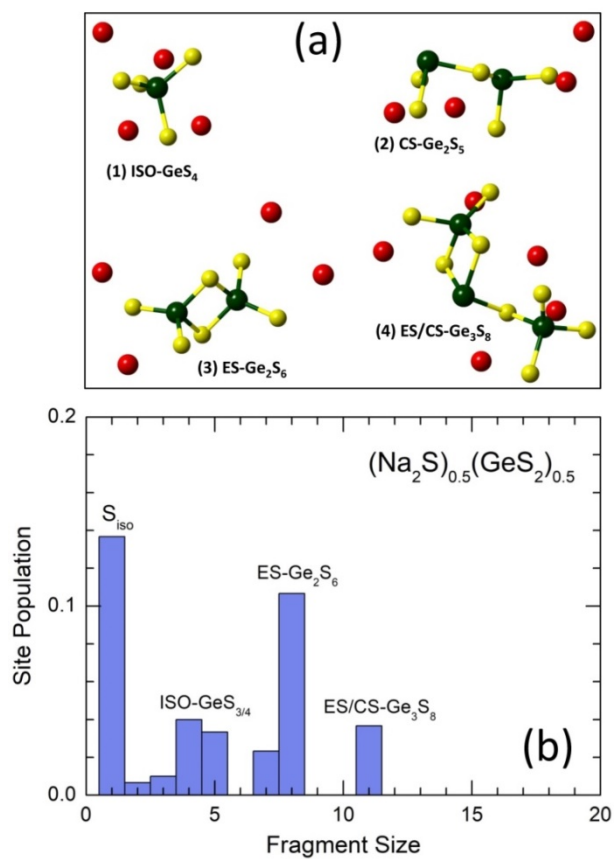


Figure S11. Small Ge-S fragments forming a disconnected Ge-S subnetwork in glassy $(\text{Na}_2\text{S})_{0.5}(\text{GeS}_2)_{0.5}$: (a) typical examples present in FPMD simulation boxes, (b) statistics of small isolated Ge-S units.

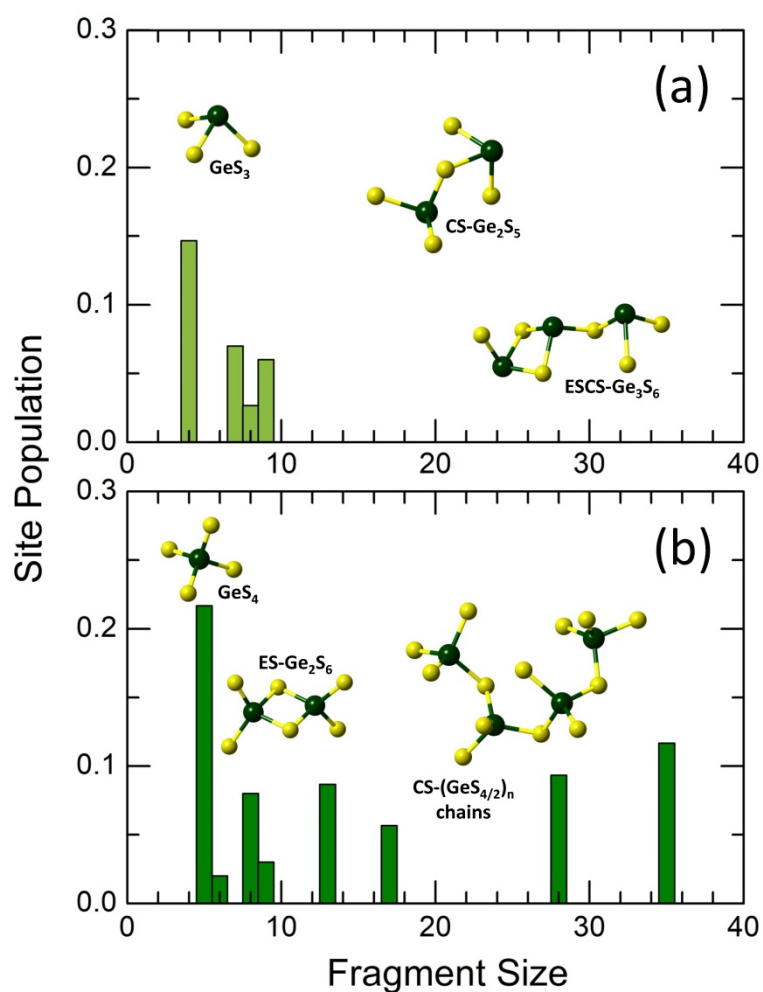


Figure S12. Connectivity of (a) Ge_{3F}-S and (b) Ge_{4F}-S subsets. The insets show typical Ge_{3F}-S and Ge_{4F}-S entities.

The three-fold coordinated germanium species are distributed rather randomly in the glass network mostly existing as isolated or connected GeS₃ pyramids and CS-Ge₂S₅ dimers ($\approx 71\%$ of the entire Ge_{3F} population), Figure S12a, with the average Ge_{3F}-Ge_{3F} separation distance of 5.7 ± 0.5 Å. In contrast, the Ge_{4F}-centered units are forming complex n -membered chains, $n \leq 35$. The fraction of small entities, isolated or connected GeS₄ or ES-Ge₂S₆, is below 45%, Figure S12b.

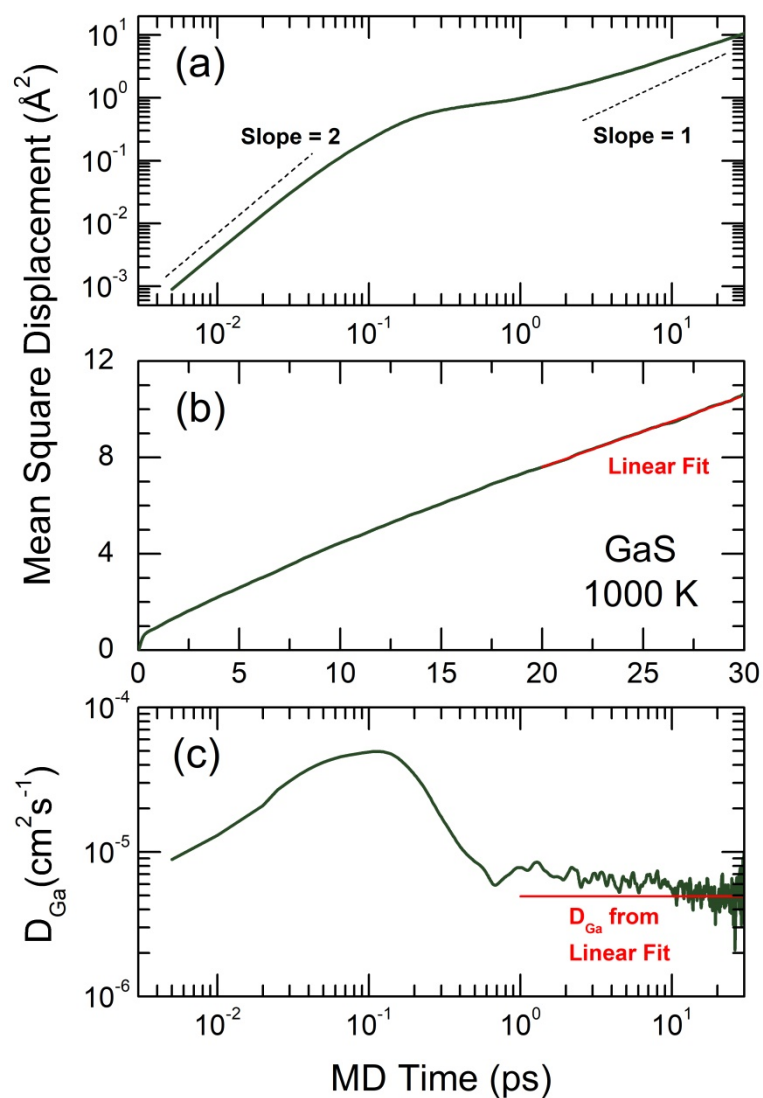


Figure S13. Gallium mean-square displacements in GaS at 1000 K:^{S14} (a) log-log scale, (b) linear scale; (c) Ga diffusion coefficients obtained by differentiation. A ballistic regime is observed below 30 fs, a diffusive motion above 20 ps. Gallium diffusion coefficient D_{Ga} , obtained by a least-square fitting between 20 and 30 ps is shown in (c) by the red solid line.

Table S1. Interatomic Distances and Bond Angles in Optimized DFT Clusters and Crystalline References

Ge-S

Cluster/Reference	Ge-S (Å)	S-Ge-S (deg)	Ge-S-Ge (deg)
Ge ₄ S ₄	2.460(1)	91.8(1)	88.2(1)
GeS ^{S12}	2.441(1)	93(2)	96.4 105.6

Na-S

Cluster/Reference	Na-S (Å)	S-S (Å)	S-Na-S (deg)	Na-S-Na (deg)
S ₂ Na ₂	2.810(5)	2.10(1)	45.9	134(1)
S ₂ Na ₃	2.809	2.15	45.0	106.3
α-Na ₂ S ₂ ^{S4}	2.818(15)	2.128	44.2(2)	106.6(1)
β-Na ₂ S ₂ ^{S4}	2.90(12)	2.158	45.2 106.2	106.2

Na-Ge-S

Cluster	Ge-S (Å)	Na-S (Å)	S-Ge-S (deg)	Ge-S-Ge (deg)	S-Na-S (deg)	Na-S-Na (deg)
Ge ₄ S ₁₀ Na ₄	2.151* 2.28(2)**	2.75(4)	109(2)	111(1)	85	–
CS-Ge ₃ S ₁₀ Na ₄ H ₂	2.18(2)* 2.298(4)**	2.78(7)	109(6)	114.4	80.3 151.5	143(16)
CS-Ge ₂ S ₇ Na ₆	2.215(1)* 2.298(1)**	2.79(5)	109(4)	116.3	85(6) 144.7	94(20) 142(10)
ES-Ge ₂ S ₆ Na ₄	2.224* 2.275**	2.81	109(7)	83.6	81.9	81.3
CS/ES-Ge ₃ S ₉ Na ₆	2.19(2)* 2.269(9)**	2.83(8)	109(10)	86.0 114.5	81(3) 112(25)	90(3) 131(9)
GeS ₄ Na ₄	2.239*	2.906	109.47	–	77.96	100.86
CS-Ge ₂ S ₆ Na ₂ H ₃	2.25(2)* 2.27(3)**	2.78(1)	109(5)	103.5	94.6(2)	84.0(4)

Table S2. Interatomic Distances and Bond Angles in Crystalline Na-Ge-S References

Reference	Ge-S (Å)	Na-S (Å)	S-Ge-S (deg)	Ge-S-Ge (deg)	S-Na-S (deg)	Na-S-Na (deg)
Na ₄ Ge ₄ S ₁₀ ^{S15}	2.139(3)*	2.88-3.34	109(2)	106.7(5)	89(14)	88(19)
	2.225(21)**				137(5)	148(12)
Na ₂ GeS ₃ ^{S13}	2.16(3)*	2.88-3.09	Figure S10		Figure 9	
	2.24(2)**					
Na ₆ Ge ₂ S ₇ ^{S16}	2.192(10)*	2.71-3.35	109(6)	113.1(2)	89(11)	86(8)
	2.262**				152(23)	163(12)

* Ge-S(*t*)

** Ge-S(*b*)

Additional References

- (S1) Bounazef-Legenne, T. *Verres de Chalcogénures Dopés au Sodium: Variété Chimique et Topologique et Relation avec les Propriétés de Transport*; Ph.D. Thesis: Université du Littoral Côte d'Opale, France, 2020.
- (S2) Bychkov, E.; Bychkov, A.; Pradel, A.; Ribes, M. Percolation Transition in Ag-doped Chalcogenide Glasses: Comparison of Classical Percolation and Dynamic Structure Models. *Solid State Ionics* **1998**, *113–115*, 691–695.
- (S3) Frischat, G. H. *Ionic Diffusion in Oxide Glasses*; Trans Tech Publications, 1975.
- (S4) Böttcher, P.; Getzschmann, J.; Keller, R. Zur Kenntnis der Dialkalimetaldichalkogenide β - Na_2S_2 , K_2S_2 , α - Rb_2S_2 , β - Rb_2S_2 , K_2Se_2 , Rb_2Se_2 , α - K_2Te_2 , β - K_2Te_2 und Rb_2Te_2 . *Z. Anorg. Allg. Chem.* **1993**, *619*, 476–478.
- (S5) Chau, P.-L.; Hardwick, A. J. A New Order Parameter for Tetrahedral Configurations. *Mol. Phys.* **1998**, *93*, 511–518.
- (S6) Errington, J. R.; Debenedetti, P. G. Relationship between Structural Order and the Anomalies of Liquid Water. *Nature* **2001**, *409*, 318–321.
- (S7) Caravati, S.; Bernasconi, M.; Kühne, T. D.; Krack, M.; Parrinello, M. Coexistence of Tetrahedral- and Octahedral-Like Sites in Amorphous Phase Change Materials. *Appl. Phys. Lett.* **2007**, *91*, No. 171906.
- (S8) Tverjanovich, A.; Khomenko, M.; Benmore, C. J.; Bokova, M.; Sokolov, A.; Fontanari, D.; Kassem, M.; Usuki, T.; Bychkov, E. Bulk Glassy GeTe_2 : A Missing Member of the Tetrahedral GeX_2 Family and a Precursor for the Next Generation of Phase-Change Materials. *Chem. Mater.* **2021**, *33*, 1031–1045.
- (S9) Bokova, M.; Tverjanovich, A.; Benmore, C. J.; Fontanari, D.; Sokolov, A.; Khomenko, M.; Kassem, M.; Ozheredov, I.; Bychkov, E. Unraveling the Atomic Structure of Bulk Binary Ga-Te Glasses with Surprising Nanotectonic Features for Phase-Change Memory Applications. *ACS Appl. Mater. Interfaces* **2021**, *13*, 37363–37379.
- (S10) Tverjanovich, A.; Khomenko, M.; Benmore, C. J.; Bereznev, S.; Sokolov, A.; Fontanari, F.; Kiselev, A.; Lotin, A.; Bychkov, E. Atypical Phase-Change Alloy Ga_2Te_3 : Atomic Structure, Incipient Nanotectonic Nuclei, and Multilevel Writing. *J. Mater. Chem. C* **2021**, *9*, 17019–17032.
- (S11) Dittmar, G.; Schaefer, H. Die Kristallstruktur von H.T.- GeS_2 . *Acta Crystallogr., Sect. B* **1975**, *31*, 2060-2064.
- (S12) Wiedemeier H.; von Schnering, H. G. Refinement of the Structures of GeS, GeSe, SnS and SnSe. *Z. Kristallogr.* **1978**, *148*, 295–303.
- (S13) Olivier-Fourcade, J.; Philippot, E.; Ribes, M.; Maurin, M. Structure Cristalline du Thiogermanate de Sodium Na_2GeS_3 . *C. R. Hebd. Séances Acad. Sci., Serie C*, **1972**, *274*, 1185-1187.
- (S14) Tverjanovich, A.; Khomenko, M.; Bereznev, S.; Fontanari, D.; Sokolov, A.; Usuki, T.; Ohara, K.; Le Coq, D.; Masselin, P.; Bychkov, E. Glassy GaS: Transparent and Unusually Rigid Thin Films for Visible to Mid-IR Memory Applications. *Phys. Chem. Chem. Phys.* **2020**, *22*, 25560–25573.
- (S15) Philippot, E.; Ribes, M.; Lindqvist, O. Structure Cristalline de $\text{Na}_4\text{Ge}_4\text{S}_{10}$. *Rev. Chim. Miner.* **1971**, *8*, 477-489.
- (S16) Jumas, J. C.; Olivier Fourcade, J.; Vermot-Gaud-Daniel, F.; Ribes, M.; Philippot, E.; Maurin, M. Etude Structurale de Thiocomposés à Groupements Anioniques de Type -Pyro-, $\text{Na}_6\text{X}_2\text{S}_7$ (X = Ge, Sn) et $\text{Ba}_3\text{Sn}_2\text{S}_7$. *Rev. Chim. Miner.* **1974**, *11*, 13-26.